Assessment of Crack in Corrosion Defects in Natural Gas Transmission Pipelines

by

Seyed Aliakbar Hosseini

A thesis
presented to the University of Waterloo
in fulfillment of the
thesis requirement for the degree of

Master of Applied Science
in
Mechanical Engineering

Waterloo, Ontario, Canada, 2010

Author's Declaration

I hereby declare that I am the sole author of this thesis. This is a true copy of the thesis, including any required final revisions, as accepted by my examiners.

I understand that my thesis may be made electronically available to the public.

Seyed Aliakbar Hosseini

Abstract

Pipelines are one of the safest forms of transportation for oil and gas. However, pipelines may experience some defects, such as cracks, corrosion and cracks in corrosion, during service period. Therefore, evaluation of these defects is very important in terms of assessment and for continued safe operation. At present, there are different assessment methods for different types of defects in pipelines. The most popular codes for crack defect assessment in oil and gas pipelines are API 579 and BS 7910, whereas the most common methods for assessing corrosion defects are RSTRENG and Modified B31G. Besides these codes and methods, there are numerical programs, such as CorLAS, which have been used successfully for assessing crack flaws in pipelines.

In this thesis, the current defect assessment methods for crack, corrosion and crack in corrosion defects are reviewed. Crack in corrosion defects (CIC) have been investigated less than crack or corrosion defects. The aim of this study was to evaluate the effect of these defects on the failure pressure of natural gas transmission pipelines. Consequently, a series of burst tests with varying defect depths were undertaken on end-capped, seam-welded API 5L Grade X60 (433 MPa yield stress) pipeline steel of external diameter 508 mm (20 inch), 5.7 mm wall thickness.

Defects were created by pre-fatiguing the pipe to create a crack. The number of cycles required to create a fatigue crack were varied between 75000 to 150000 cycles based on the desired final defect depth. For artificial corrosion defects, Rectangular grooves were machined on the outside of the pipe. The corners of these rectangular grooves were rounded to decrease the stress concentration. For the (CIC) defects, the pipe was pre-fatigued to create a sharp crack, and the artificial corrosion defect was simulated by machining a rectangular groove over the fatigue crack. The depth of the artificial corrosion defect was same as the depth of the initial cut. The rupture tests were conducted by pressurizing the pipe until failure occurred.

Results were analyzed using various assessment methods. For the artificial corrosion defects, the predicted failure pressures based on RSTRENG were more reliable than those based on Modified B31G.

This study revealed that CorLAS provided the least conservative prediction for crack defects with an average error of 18% of the experimental, whereas the other methods provided more conservative estimates of failure pressure. Moreover, the predicted failure pressure of the level 3 FAD for API 579 cylinder equations had better agreement with experimental results in comparison with the other methods, i.e. BS7910 and NG-18.

The failure pressure for CIC defects for pipes tested fell between corrosion defects (lower bound) and crack defects (upper bound). The transition to crack defect behavior only occurs when the crack defect depth is significant or vice versa. It should be noted that the crack to corrosion ratio is not the only parameter to evaluate a CIC defect. There are other parameters such as total defect depth and defect profile, which affect the failure behavior of a CIC defect.

Acknowledgments

I am heartily thankful to my supervisors, Professor Duane Cronin and Professor Alan Plumtree, whose encouragement, guidance and support from the initial to the final level enabled me to develop an understanding of the subject.

I would like also thank to Tom Gawel, Andy Barber, John Bolt, Norval Wilhelm and other staff in machine shop for their technical support, advice and expertise.

I would also acknowledge to Behzad Behravesh, Keivan Ahmadi and Badr Bediari for their friendship and help over the past two years.

The author gratefully acknowledges financial support from Trans Canada Pipelines Incorporation.

Finally, I am particularly indebted to my wife and best friend Mina, as without her patience, support and encouragement this study may never have ended.

Table of Contents

List of Figures

List of Tables

List of Symbols

α	Material coefficient for the Ramberg-Osgood relationship
a	Crack depth
A	Fracture area of the Charpy specimen
A_0	Crack defect area
B	Material thickness
C	Paris constant
c	½ Crack or corrosion length in longitudinal direction
c_{eq}	Crack half length
$CVNc_V$	CVN Charpy fracture energy
CVN^S	Sub-size specimen Charpy impact energy
CVN_{US}	Specimen Charpy upper impact energy
CVN_{US}^S	Sub-size specimen Charpy upper impact energy
d	Defect depth
D	Pipe diameter
δ	Crack-tip opening displacement
δ_V	Side deflection (parallel to the external load)
δ_H	Side deflection (transverse to the external load)
ΔK	Stress intensity range
e	Engineering strain
E	Elasticity modulus
E'	Elasticity modulus for plane strain
ϵ	Total strain
ε_{ref}	Reference strain

ϵ_e	Elastic strain
ϵ_p	Plastic strain
ε_T	True strain
G	Arbitrary load or moment applied to the system
Γ	Arbitrary path enclosing the crack tip
H	Horizontal force applying on the pipe
J	J integral
J_c	Fracture toughness in J-integral terms determined at the point of instability
K_I	Stress Intensity
(K_{IC})	Fracture toughness of material
K_{th}	Threshold stress intensity
K_{mat}	Lower bound estimate for fracture toughness of material
K_{r}	Ordinate of the failure assessment diagram (FAD) (=K_I / K_{c})
L_r^P	Abscissa of the failure assessment diagram (FAD Level 2 &3) (=σ_{ref}^P / σ_Y)
L	Length of corroded area
m	Paris constant
M_0	Bending moment
$\mathrm{M_p}$	Bulging factor
M	Folias bulging factor
M_{Max}	maximum bending moment
P_f	Failure pressure
R	Pipe radius
s	Arc length in J-integral contour
S_r	Abscissa of the failure assessment diagram (FAD Level 1) (=σ_{ref}^P / σ_{flow})
σ_{h}	Hoop stress

σ_{m}	Nominal stress
σ_Y	Yield strength
σ_T	True stress
σ_u	Ultimate tensile strength
σ_{Eng}	Engineering stress
σ_{ref}^P	Reference stress
$\overline{\sigma}$	Flow stress
t	Pipe wall thickness
t_c	Thickness of the full-size specimen
t_c^s	Thickness of the sub-size specimen
T	Traction vector
u	Displacement vector
U	Strain energy
V	Vertical force applying on the pipe
w	the strain energy density
Y	Dimensionless geometrical factor

1. Introduction

There are many pipelines in service around the world. Pipelines are the most common and feasible method for transporting oil and gas because of the volume that can be transported. For instance, pipelines transport 97% of the oil and natural gas produced in Canada [1] and nearly two-thirds of the oil annually produced in the USA [1]. Canada is the largest supplier of crude oil to the United States and is the second largest global exporter of natural gas, and the value of this exported natural gas was approximately $27.8 billion in 2005 [1]. Furthermore, it is essential that pipeline assets must double in size by 2015 to meet forecast production increases [1]. In general, pipelines may become defective during service period. Pipeline defects resulting of coating or cathodic protection degradation, local environment or third party damage during fabrication. Evaluation of these defects is important for pipeline companies in terms of assessment and continued operation. The more the pipeline ages, the more integrity assessment is required.

Before the advent of modern and high resolution inspection devices, pipeline inspectors selected sections of the pipeline randomly and inspected them to determine whether there was a defect or not. At present, pipeline inspectors are able to scan their line with high resolution inspection tools. It should be noted that all defects in pipelines are not critical and do not need to be repaired. Therefore, pipeline companies need to determine critical defect dimensions for making decisions about repairing the defects or leaving them for further service.

Based on the type of defect, there are different codes and standards for assessing a defect in pipelines. For instance, the most popular codes for crack defect assessment in oil and gas pipelines are API 579 [3] and BS7910 [4] and the most common methods for corrosion assessment defects are RSTRENG and Modified B31G [5]. Besides these codes and methods, there are some other numerical programs, such as CorLAS, which have been used successfully for assessing cracks in pipelines [6, 7].

In general, significant corrosion defects (i.e. greater than 10% of the wall thickness) in depth and crack-type defects are not found together. This may in part be related to the required soil chemistry to generate each type of defect. However, recently these hybrid defects including cracking within corrosion have been identified [7].

In terms of assessment, crack in corrosion defects (CIC) have not been investigated extensively. Therefore, the primary goals of this study are:

- Literature review concerning existing methods to evaluate crack only and corrosion only defects.
- Literature review concerning existing experimental data to validate the approaches for evaluation of CIC defects.
- Material characterization to provide important data for crack, corrosion and CIC evaluation.
- Assuming CIC defects behave as crack only defects and comparing the NG-18 method, Level 3 FAD (K approach) and CorLAS for predicting collapse pressure of the CIC defects.
- Assuming CIC defects behave as corrosion only defects and comparing the RSTRENG and Modified B31G for predicting collapse pressure of the CIC defects.

Even though an understanding of the mechanism and environmental or mechanical conditions required to generate these defects is important, the aim of this study was to review existing techniques for crack evaluation and to provide a framework for application of these techniques to cracking within corrosion defects. For the purpose of this study, several assumptions were made:

- CIC defects are located in the pipe body away from seam or girth welds.
- The local material properties may be taken as those of the pipe body. There are no local reductions in properties (fracture toughness, strength, and ductility) due to the presence of the defect or environment.
- Fatigue growth of the crack was not considered.

With respect to organization of the thesis, Chapter 2 reviews the current defect assessment methods and codes of crack, corrosion and CIC defects. The material characterization procedures can be found in Chapter 3. Specific details of the experimental procedures utilized at this study are given at Chapter 4. Chapter 5 outlines the results of the current study and concluding statements and some recommendations for future works are provided at Chapter 6.

2. Background

Crack in corrosion defects (CIC) may occur in oil and gas pipelines during their service period. These type of defects were first discovered in 1960s in the southern USA [8]. In general, CIC defects are found in areas on the pipeline where there is no cathodic protection or the coating has failed [8].

Although crack and corrosion defects have been investigated extensively, CIC defects are relatively new and have not been reviewed the same amount of integrity.

A study by Cronin and Plumtree [9] was done to determine the behavior of long cracks within long corrosion grooves for these hybrid defects. The study concluded that the behavior of these hybrid defects fell between pure crack and pure corrosion defects. Furthermore, it was found that the transition to pure corrosion defect behavior occurred when the corrosion defect depth was greater than 75% of the total defect depth [9].

In the following sections, the background for corrosion and crack defects will be reviewed.

2.1 Corrosion Defects

2.1.1 Corrosion Morphology

Corrosion is the degradation of the material due to chemical or electrochemical interactions with their environments. Corrosion may be classified in six categories in pipelines as follows [10]:

- **Pitting**

Results in a localized, deep penetration of the metal surface with little general corrosion in the surrounding area.

- **Crevice corrosion**

Occurs in or immediately around places with gaskets, bolts and lap joints where crevice exists.

- **Uniform or general corrosion**

The corrosion rate proceeds at approximately the same rate over the whole surface being corroded and the extent can be measured as mass loss per unit area.

- **Inter granular corrosion**

Results in corrosion at or near the grain boundaries of the metal.

- **Erosion Corrosion**

This requires conjoint erosion and corrosion that typically occurs in fast flowing liquids that have a high level of turbulence.

2.1.2 Causes of Corrosion

Corrosion defects at the external surface of pipelines (Figure 2.1) are often the result of fabrication faults, coating or cathodic protection issues, residual stress, cyclic loading, temperature or local environment (soil chemistry).In general, corrosion may occur in most pipes due to coating failure, and a pipe without any protective coating will experience external corrosion after some years. However, corrosion can occur on the internal surface of the pipeline due to contaminants in the products such as small sand particles or amino acids.

Figure 2.1- A Corroded Pipe

2.1.3 Important Parameters in Corrosion Defects

There are some parameters, which have been recognized as significant in the remaining strength of corroded pipe. The parameters in order of significance are [11]:

- Internal pressure
- Pipe diameter
- Wall thickness/defect depth
- Defect length/width
- Ultimate strength
- Yield strength/strain hardening characteristics
- Fracture (Charpy) toughness

It should be taken into account that fracture toughness properties of new pipelines materials are high; therefore, this parameter does not generally play a significant role in corroded pipes [12].

2.1.4 Current Assessment Methods

There are many methods for assessing corrosion defects in pipelines. At present both RSTRENG and the Modified B31G are the most commonly used methods for assessing corroded defects in pipeline operators. All of the above methods are based on the NG-18 equation for failure of part-wall flaw, but differ in approximation of the Folias factor [5], flow stress and the defect profile [5]. The Folias factor (M) is a term that describes the bulging effect of a shell surface that is thinner in wall thickness than surrounding shell.

Due to the complicated geometry of corroded pipes, there is no exact analytical stress analysis for these kinds of pipes. However, finite element methods have been used successfully to predict the failure pressure of a corroded pipe [11].

Modified B31G

The B31G criterion is based on the determining of the effect of the corroded defect on the hoop stress of a pipe [1]. Conservatism of the original B31G criterion leads to extreme repairs or replacement of pipes. Therefore, a modified form of B31G was developed. B31G assumes the corroded area as having a parabolic shape (2/3 dL, but Modified B31G assumes arbitrary area by 0.85 dL. Based on the Modified B31G criterion, the hoop stress, which is the maximum principal stress in the plane pipe, controls the failure in the pipe. There is a direct relation between flow stress, bulging factor (M) or Folias factor and defect geometry according to the NG-18 surface flaw equation [5]:

$$\sigma_\theta = \overline{\sigma}\left[\frac{1-\frac{d}{t}}{1-\left(\frac{d}{t}\right)\frac{1}{M}}\right] \tag{2.1}$$

For Modified B31G the above equation can be written as:

$$\sigma_\theta = \overline{\sigma}\left[\frac{1-0.85\frac{d}{t}}{1-0.85\left(\frac{d}{t}\right)\frac{1}{M}}\right] \tag{2.2}$$

where

$\overline{\sigma}(flow\ stress) = \sigma_y + 10\ (ksi)$ =$\sigma_y + 69.8\ (MPa)$

$$M = \sqrt{1+0.6275\left(\frac{2c}{\sqrt{Dt}}\right)^2 - 0.003375\left(\frac{2c}{\sqrt{Dt}}\right)^4} \tag{2.3}$$

Equation 2.2 calculates the failure stress of a corroded pipe under internal pressure containing an axial corrosion defect, oriented along the axis of the pipe. The failure pressure can be calculated using:

$$P_f = (\frac{t}{R})\overline{\sigma}\left[\frac{1-0.85\frac{d}{t}}{1-0.85\left(\frac{d}{t}\right)\frac{1}{M}}\right] \tag{2.4}$$

It should be noted that equation (2.4) underestimates the remaining strength of the pipe. First, it assumes that the corrosion areas are aligned in the axial direction of the pipe. However as shown in Figure 2.2 and Figure 2.3, the line connecting the corroded pits is projected onto the longitudinal axis of the pipe.

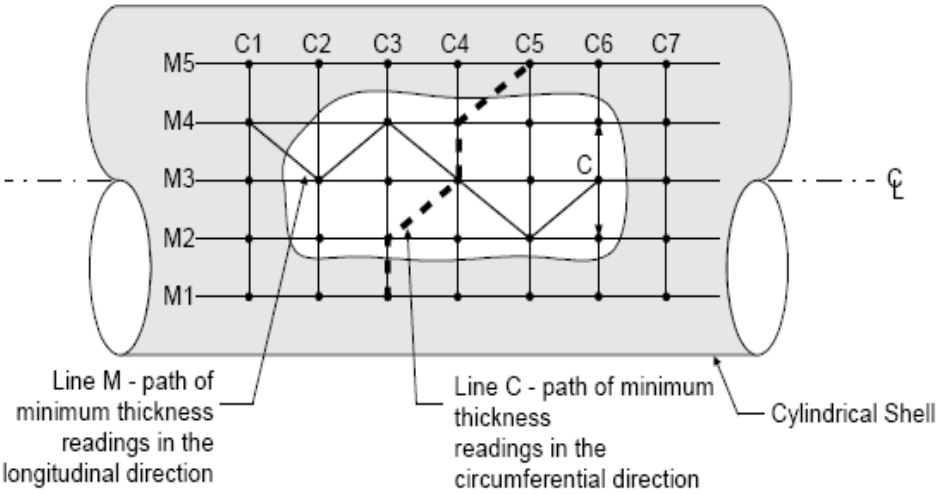

Figure 2.2- Inspection Planes and the Critical Thickness Profile [1]

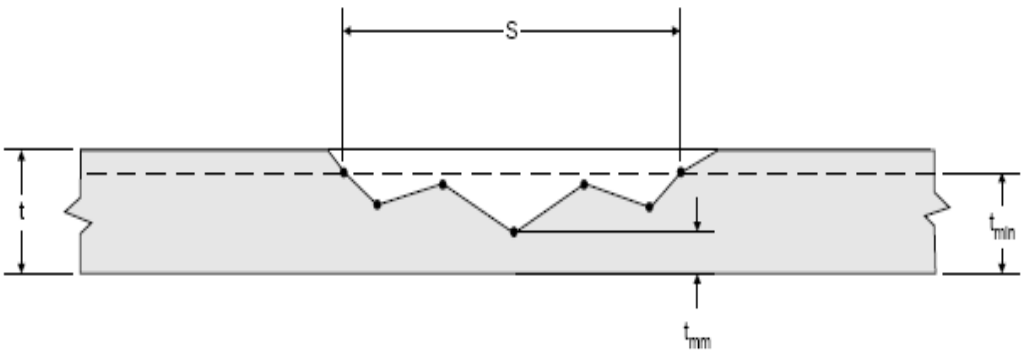

Figure 2.3- Critical Thickness Profile (CTP) - Longitudinal Plane (Projection of Line M) [1]

Secondly, Modified B31G assumes that the corrosion pits are blunt defects in comparison with other defects such as cracks. It has been shown sharp surface flaws have significantly lower failure pressure than blunt surface defects. Moreover, equation 2.4 was developed on the data of burst tests of pipes containing sharp flaws [5]. Hence, equation 2.4 gives conservative predictions.

❖ **RSTRENG**

RSTRENG is the preferred method for predicting the remaining strength of pipes containing external corrosion, as it is less conservative than Modified B31G and provides a more accurate representation of the corroded area [13] . This method also uses the modified form of the NG18 equation (Equation 2.1). The difference between Modified B31G and RSTRENG is the projected area. Modified B31G calculates the remaining strength based on the parabolic area (0.85 L*d) of the corroded area, whereas RSTRENG uses an effective area method. Therefore, RSTRENG calculates the defect area more accurate than Modified B31G [13]. Figure 2.4 compares these two methods for estimating the corrosion profile.

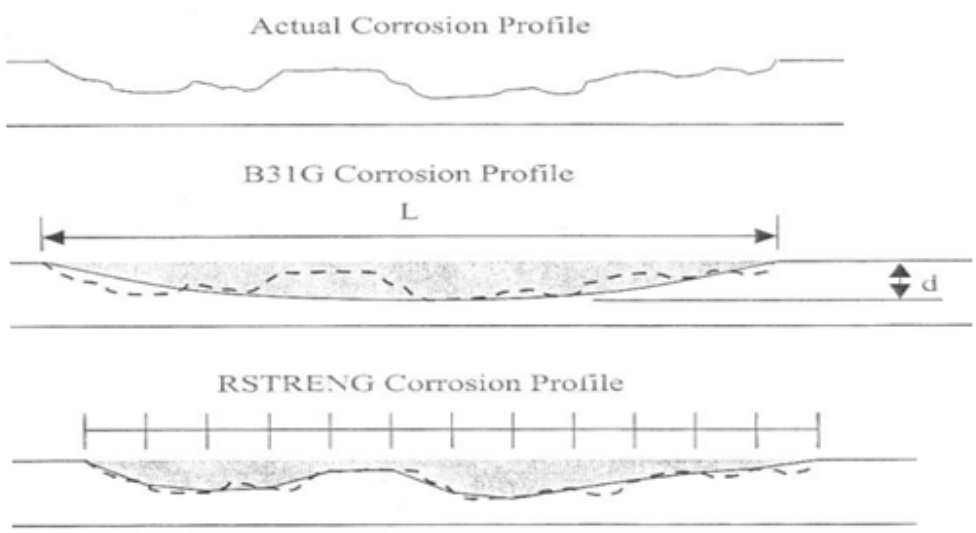

Figure 2.4- Corrosion Defect Profile [11]

In the effective area method, each individual measurement is assessed in combination with other corroded areas in an iterative procedure. For example, the number of calculations for prediction of the failure pressure in a pipe for seven measurements is 21. Figure 2.5 illustrates these iterations for predicting the lowest failure pressure.

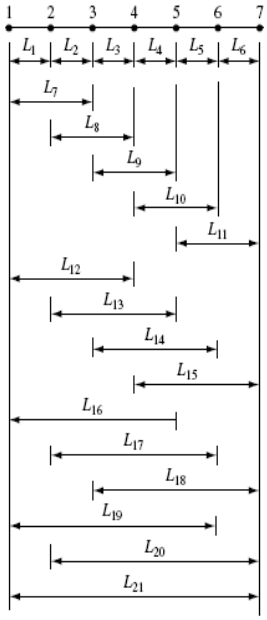

Figure 2.5- RSTRENG Performs 21 computations For 7 Measurements Readings [1]

According to Figure 2.5, for seven pit depths, RSTRENG performs twenty-one iterative computations of the failure pressure using equation 2.5. The lowest value is the minimum failure pressure [1].

$$P_f = (\frac{t}{R})\overline{\sigma}\left[\frac{1-\frac{A}{A_0}}{1-\frac{A}{A_0}\frac{1}{M}}\right] \tag{2.5}$$

A comparison between RSTRENG, Modified B31G and B31G is given in Table 2.1.

Table 2.1- Comparing Different Methods for assessing the Burst Strength of a Corroded Area

Method	Basic Equation.	Flow Stress	Defect Shape	Bulging Factor (M)
B31G	NG18 (Eq.2.1)	$1.1\sigma_y$	Parabolic 2/3 (d/t)	$M = \sqrt{1+0.8\left(\frac{2C}{\sqrt{Dt}}\right)^2}$
M B31G	NG18 (Eq.2.1)	$\sigma_y + 69.8\ \text{MPa}$	Arbitrary 0.85 (d/t)	$M = \sqrt{1+0.6275\left(\frac{2C}{\sqrt{Dt}}\right)^2 - 0.003375\left(\frac{2C}{\sqrt{Dt}}\right)^4}$
RSTRENG	NG18 (Eq.2.1)	$\sigma_y + 69.8\ \text{MPa}$	Effective Area	$M = \sqrt{1+0.6275\left(\frac{2C}{\sqrt{Dt}}\right)^2 - 0.003375\left(\frac{2C}{\sqrt{Dt}}\right)^4}$

2.2 Crack Defects

2.2.1 Cause of Crack Defects

Cracks in high pressure pipelines may result from the interaction of susceptible metallic material, tensile stress and an aggressive electrolyte.

The crack characteristics can vary greatly depending on the cause of the crack, the material, and the environment. Cracks can initiate on the external pipeline surface and grow in both the depth and surface directions. Growth along the surface is perpendicular to the hoop stress, resulting in crack alignment along the axial axis of the pipeline [8].

2.2.2 Crack Defect Evaluation

There are several common methods for assessing crack defects in pipelines. These methods use linear elastic fracture mechanics (LEFM) or elastic-plastic fracture mechanics (EPFM). LEFM cannot be used when significant yielding occurs prior to fracture. In general, the maximum stress intensity occurs in the deepest point of a semi-elliptical crack in plane strain conditions. Depending on the material properties, loading conditions and defect shape and size, crack defects may fail by fracture or by plastic collapse.

- **Linear Elastic Failure Mechanics (LEFM)**

LEFM can be used when crack-tip plasticity is small. In general, the LEFM method can be used when the material toughness is low (brittle) and the stress intensity at the crack-tip is high. The linear elastic stress intensity factor (K) for mode I loading (Figure 2.6) is expressed as follow:

$$K_I = \mathrm{Y}\sigma_{\mathrm{m}}\sqrt{\pi a} \tag{2.6}$$

The geometrical factor can be calculated using handbooks and codes such as stress intensity factors handbook [14]. This factor accounts for the effect of

geometry of crack and the body, the boundary conditions and the type of loading. The linear elastic stress intensity can be calculated for any combination of σ and a.

Figure 2.6- Mode I(opening) [15]

The fracture toughness should be used to assess of the crack flaw in a component. K_I should be computed based on the crack dimension in a component under load and the results compared with the value of fracture toughness. Fracture toughness is a material property and, based on definition, when the critical value of K_I is reached(K_c), fracture occurs. K_I and K_c should be applied where brittle fracture occurs.

❖ Elastic Plastic Failure Mechanics (EPFM)

EPFM is an advanced approach to evaluate a component with crack-like flaws, when there is a significant plastic zone at crack tip. This method uses two parameters the J and sum of strain energy density (U). The J integral is defined as a path independent integral around the crack tip. In other words, the J integral is the rate of change of potential energy between two points along the crack tip (a) and (a+Δa) or crack growth. In this context:

$$J = -\frac{1}{B}\frac{\partial U}{\partial a} \tag{2.7}$$

Since pipeline materials are typically ductile, J and J_c should be applied for assessing the crack flaws.

The J_c can be applied to estimate the equivalent value of K_c as follows:

$$K_c = \sqrt{J_c\, E'} \tag{2.8}$$

where

For plane strain $E' = \frac{E}{1-\nu^2}$

Equation 2.8 can be used when there is a small plastic zone at the crack tip or small scale of yielding at the crack tip. According to equation 2.9, the J value includes an elastic and plastic part, therefore the elastic part of J value can be used in equation 2.8 (i.e. $J_c = J_{el}$).

$$J = J_{el} + J_{pl} \tag{2.9}$$

2.3 Assessment Methods for Crack-Like Flaws

There are several assessment methods for crack-like defects in pipelines including API 579, BS7910, NG18 and software applications such as CorLAS. All have been used successfully to evaluate crack defects, but the degree of conservatism and sensitivity to the various input parameters is not known.

2.3.1 Failure Assessment Diagram (FAD)

The failure assessment diagram (FAD) is widely used for assessing crack-like flaws in pipelines.

The FAD approach can be used for a wide range of material behaviors, from brittle fracture under LEFM conditions to ductile fully plastic collapse in three deferent levels. The FAD approach can also be used for welded components [15].

- **Level 1 FAD**

The simplest level of FAD, where there is limited information on the material properties or loading conditions, is level 1. This is shown in Figure 2.7. The crack defect is considered acceptable if K_r is less than 0.707 and S_r is less than 0.8. If the assessment point lies in the area within the assessment line, the crack is

acceptable. Otherwise it is not. It should be noted that K_r and S_r are toughness ratios and parameters for plastic collapse. These are shown in Equations 2.10 and 2.11.

$$K_r = \frac{K_I}{K_c} \tag{2.10}$$

$$S_r = \frac{\sigma_{ref}^P}{\sigma_{flow}} \tag{2.11}$$

where

$\sigma_{flow} = \frac{\sigma_Y + \sigma_u}{2} \leq 1.2\sigma_Y$

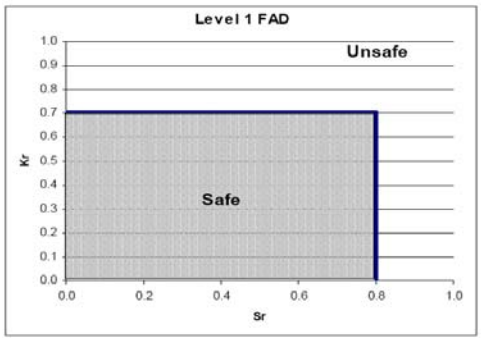

Figure 2.7- Failure Assessment Diagram (Level 1) [7]

The calculation procedures for K_r and S_r (Level 1) applied to API579 and BS7910 are explained in detail in Appendices A and B respectively.

- **Level 2 FAD**

The level 2 FAD provides a better estimate of the structural integrity of a component than a Level 1 assessment with a crack-like flaw [1] because Level 1 is based on the assumption of an elastic-perfectly plastic stress-strain curve with no strain hardening. Level 2 and Level 3 allow more by using the actual shape of the material stress-strain curve [4]. The assessment line is given by equation 2.12 and if the assessment point lies within the area bounded by the axes and the assessment line, the flaw is acceptable otherwise it is not. This is shown in Figure 2.8.

$$K_r = (1 - 0.14\left(L_r^P\right)^2\left(0.3 + 0.7\exp\left[-0.65\left(L_r^P\right)^6\right]\right) \tag{2.12}$$

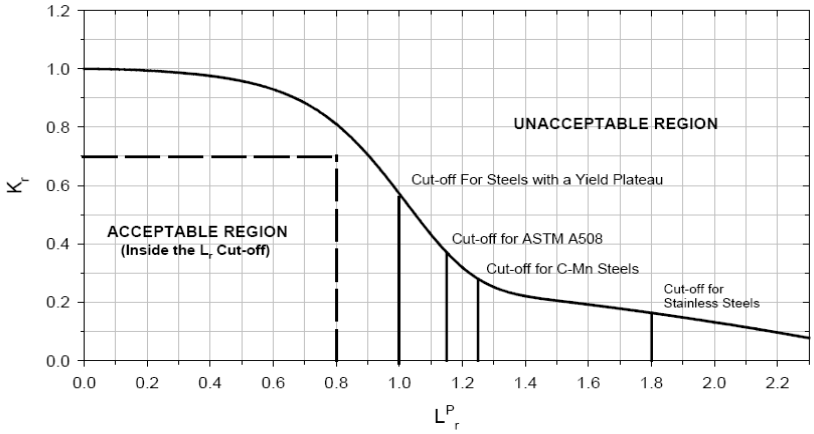

Figure 2.8- Failure Assessment Diagram (Level 2) [1]

The limiting Cut-off line ($L_{r(\max)}^P$) is to prevent localized plastic collapse and is calculated as follows [3]:

$$L_{r(\max)}^{\mathrm{p}} = \frac{\sigma_y + \sigma_u}{2\sigma_{ys}} \tag{2.13}$$

- **Level 3 FAD**

The assessment procedure in Level 3 FAD provides the best estimate of the structural integrity of a component with a crack-like flaw [1]. It requires a true stress-strain curve of the material containing the flaw. The assessment line is given by equation 2.14 and if the assessment point lies within the area bounded by the axes and the assessment line, the flaw is acceptable otherwise it is not acceptable.

$$K_r = [\frac{E\varepsilon_{ref}}{L_r^P\sigma_Y} + \frac{\left(L_r^P\right)^3\sigma_Y}{2E\varepsilon_{ref}}]^{-0.5} \tag{2.14}$$

A typical FAD Level 3 is shown in Figure 2.9.

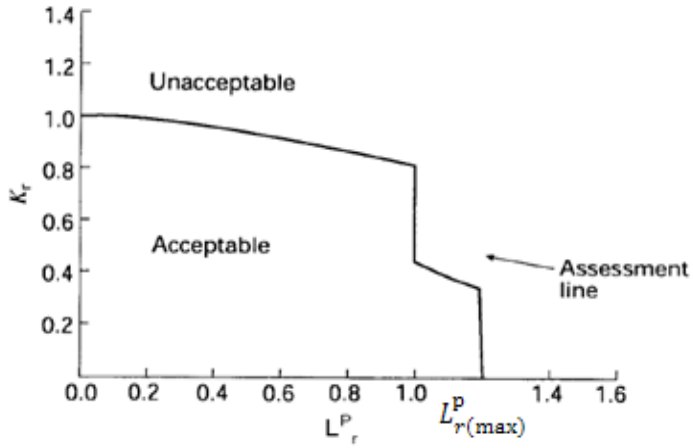

Figure 2.9- Failure Assessment Diagram (Level 3)(derived from material stress-strain data) [4]

The difference between API 579 and BS 7910 methods is in the calculation procedure for the reference stress and stress intensity. The calculation procedures for K_r and L_r^P (Level 2 and Level 3) for both API579 and BS7910 are explained in detail in Appendixes A and B respectively.

The FAD curve is divided into three regions (Figure2.10): small-scale yielding contained yielding and plastic collapse [16].

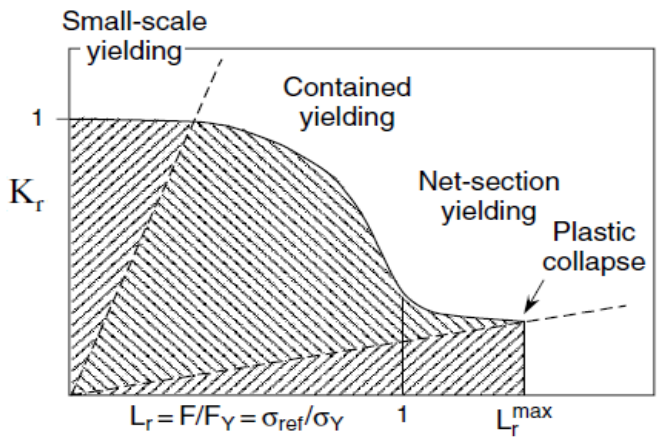

Figure2.10- Ligament Yielding Range [16]

It can be determined whether a cracked component fails by brittle fracture, contained yielding or plastic collapse based on Figure2.10.

2.3.2 NG-18 Crack Assessment Method

The NG-18 approach can be used to evaluate a crack or crack like defects in pipelines. The NG-18 equation incorporates the flow stress and fracture toughness or Charpy fracture energy (CVN) to evaluate the failure pressure in pipeline as follows[6]:

$$K_c^2 = (\frac{E\,C_v}{A})^2 = \frac{8}{\pi} c_{eq} \times \sigma_f^2 \times \ln\sec(\frac{\pi \times M_p \sigma_h}{2\sigma_f}) \quad (2.15)$$

Where

$$\sigma_f = \sigma_y + 68.9 \text{ (MPa)}$$

$$M_p = \frac{1-\frac{d}{t}(\frac{1}{M_t})}{1-\frac{d}{t}}$$

$$M_t = \sqrt{[1 + 1.255\left(\frac{c_{eq}{}^2}{Rt}\right) - 0.0135\left(\frac{c_{eq}{}^4}{R^2t^2}\right)]}$$

The failure pressure can be calculated as follows:

$$P_f = \frac{2t}{D\pi M_p} \times \sigma_f \times Cos^{-1}(\frac{1}{e^{\frac{E\pi C_V}{8AC_{eq}\sigma_f^2}}})$$

2.3.3 CorLAS

CorLAS is life prediction software developed by CC Technologies [17]. It evaluates the residual strength of pipelines containing corrosion or stress-corrosion cracking (SCC), stating “that the critical flaw size for the fracture-toughness failure criterion may be determined in one of two ways using the J integral. The first method involves computing the condition for which the applied value of J integral (J_{ap}) is equal to the J fracture toughness (J_C) of the material. When J_C is applied, the condition for initiation of tearing (crack advance) is predicted. However, if J_C is taken to be the maximum toughness, the condition for failure or tearing instability can then be predicted. This second method involves computing the tearing instability condition where the applied tearing parameter (dJ_{ap}/da) is equal to the

tearing resistance (dJ/da) of the material, and is illustrated in Fig. 2. Both methods require iterative calculations to determine the critical flaw size" [18].

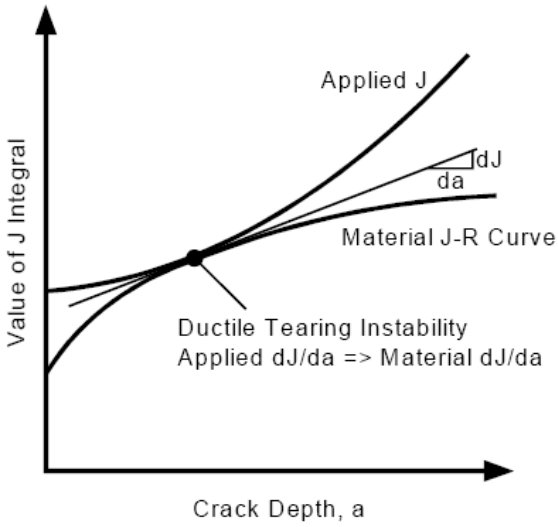

Figure2.11- Illustration of Tearing Instability Criterion [18]

For the surface crack, the following equation is used to compute values of applied J as a function of crack size (a) and stress (σ):

$$J = Q_f F_{sf}[\frac{\sigma^2 \pi a}{E} + f_3(n) a\, \epsilon_p \sigma] \tag{2.16}$$

Q_f is the elliptical shape factor, F_{sf} is the free surface factor and σ is the applied stress, and $f_3(n)$ [19] is the function developed by Shin and Hutchinson [19]. The J value either is measured from laboratory test or is the estimated Charpy energy using empirical equation 2.16, given above.

3. Material Characterization

3.1 Material Properties

Pipe material plain carbon API 5L Grade X60 pipeline steel was used in this investigation. Tensile test and Charpy impact tests were undertaken to evaluate the material properties.

3.1.1 Tensile Test

Evaluating defects in pipelines requires the use of the material stress-strain curve. This is typically achieved through uniaxial tensile tests. Twelve longitudinal and twelve circumferential specimens were tested based on ASTM (E 8M-07) procedure [20]. The thickness of the specimens was 5.7 mm, the same as wall thickness of the pipe, and the width of the specimen was 12.5 mm. The yield strength was calculated based on 0.5% strain offset [21]. The modulus of elasticity was assumed to be 207 GPa. The circumferential values were used in the assessment methods because the hoop stress is the highest stress in the pipe. A sample specimen and the specimen dimension are shown in Figure 3.1 and Figure 3.2, respectively.

Figure 3.1- A sample Tensile Test Specimen

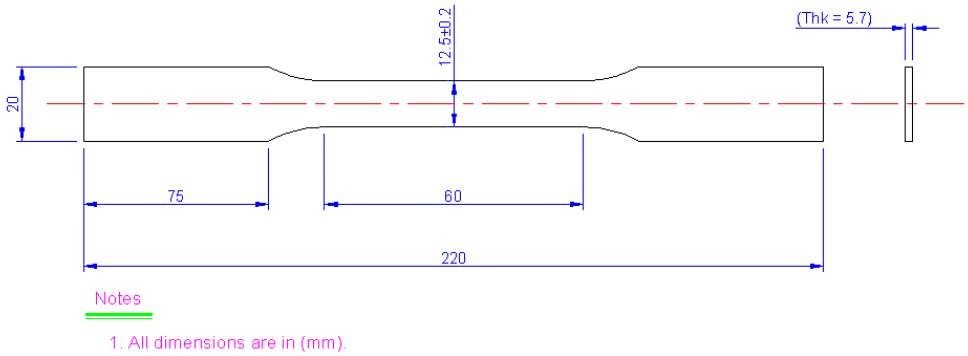

Figure 3.2- Specimen Dimensions for Tensile Test

The relation between the engineering strain and true strain is given by equation 3.1:

$$\varepsilon_T = \ln(1 + e) \tag{3.1}$$

True stress can be calculated from the engineering stress by using equation 3.2:

$$\sigma_T = \sigma_{Eng}(1 + e) \tag{3.2}$$

The above equations are only valid up to necking. At necking the strain is no longer uniform throughout the gage length.

The engineering and true stress-strain curves for specimen are shown in Figure 3.3.

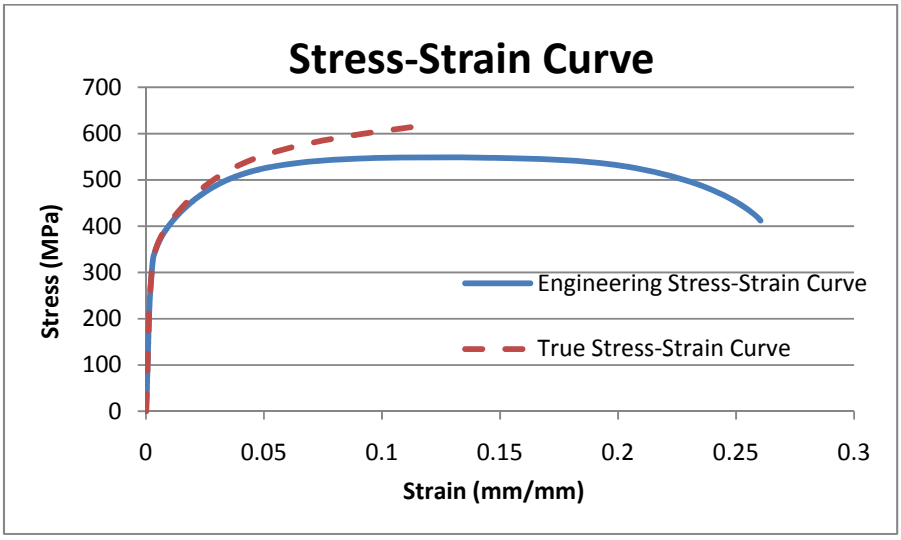

Figure 3.3- The Engineering and True Stress-Strain Curves in Circumferential Direction for One of Specimens

The Ramberg-Osgood equation (Equation 3.3) was used to describe the non linear relationship between stress and strain. This equation is based on total elastic and plastic strain.

The true stress-strain curve along the circumference axis is plotted in Figure 3.4 by using the tensile test results along the circumference axis with Ramberg-Osgood equation.

$$\epsilon = \epsilon_e + \epsilon_p$$
$$\varepsilon = \frac{\sigma}{E} + \alpha \left(\frac{\sigma}{\sigma_{Ys}}\right)^n \left(\frac{\sigma}{E}\right) \tag{3.3}$$

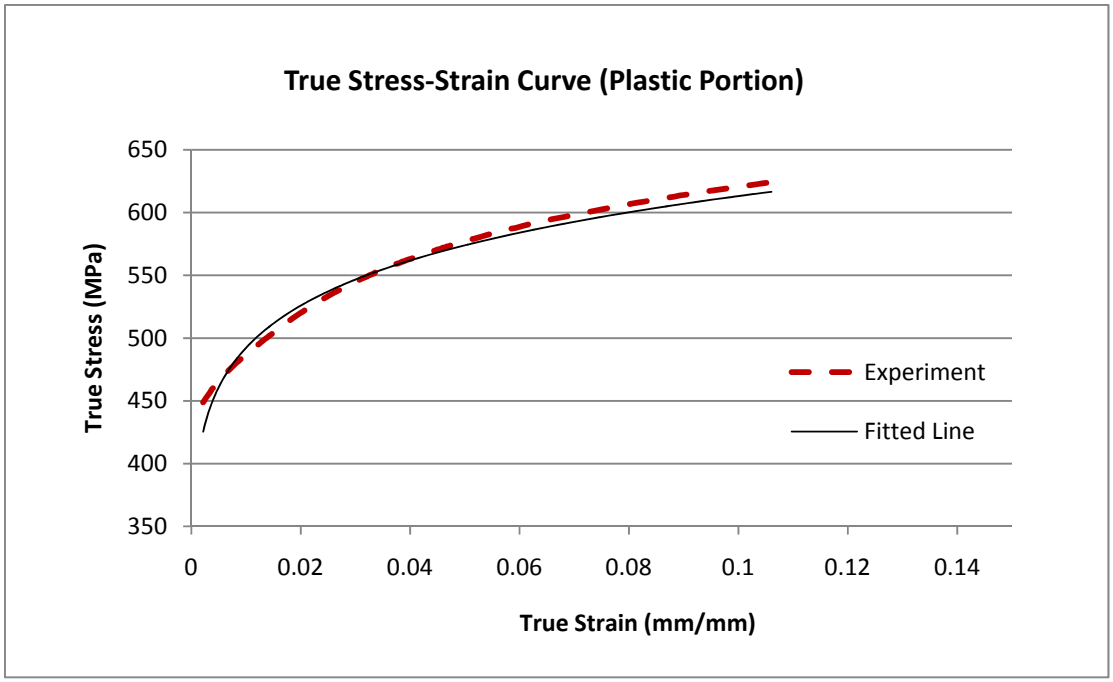

Figure 3.4- The True Stress-Strain Curves in Circumferential Direction for One of Specimens [24]

The yield strength was calculated from the engineering stress-strain curve by using the 0.5% strain offset method. The constants α and n are the strength coefficient and strain hardening, respectively.

The measured material properties are summarized in Table 3.1. The true stress-strain curve for some samples is shown in Figure 3.5.

Table 3.1- Experimental Database Material and Ramberg-Osgood Parameters [24]

Longitudinal Direction						
Specimen Id	YS (0.2 % Offset)		YS (0.5 % Offset)		UTS (Eng. Stress)	
	(MPa)	(psi)	(MPa)	(psi)	(MPa)	(psi)
L1	343	49748	361	52359	549	79626
L2	348	50473	362	52504	546	79191
L3	341	49458	356	51633	544	78900
L4	363	52649	380	55114	563	81656
L5	357	51778	380	55114	571	82817
L6	363	52649	381	55259	551	79916
L7	343	49748	361	52359	544	78901
L8	362	52504	376	54534	545	79046
L9	355	51488	372	53954	553	80206
L10	374	54244	387	56130	555	80496
L11	349	50618	365	52939	554	80351
L12	362	52504	383	55549	552	80061
Average	**355**	**51488**	**372**	**53954**	**552**	**80097**

Circumferential Direction						
Specimen Id	YS (0.2 % Offset)		YS (0.5 % Offset)		UTS (Eng. Stress)	
	(MPa)	(psi)	(MPa)	(psi)	(MPa)	(psi)
C1	480	69618	483	69908	568	82381
C2	445	64542	449	65122	560	81221
C3	454	65992	460	66717	563	81656
C4	413	59928	430	62395	579	83977
C5	424	61524	435	63091	569	82526
C6	394	57171	409	59320	565	81946
C7	407	59057	419	60771	549	79626
C8	384	55720	398	57725	539	78175
C9	398	57751	411	59611	545	79046
C10	430	62395	448	64977	590	85572
C11	423	61379	434	62946	557	70198
C12	394	57171	418	60626	561	81366
Average	**421**	**60988**	**433**	**62777**	**562**	**81511**

Ramberg-Osgood Material Parameters						
Circumferential Direction						
Specimen Id	YS (0.5 % Offset)		UTS (True Stress)		α	n
	(MPa)	(psi)	(MPa)	(psi)		
C1	483	69908	631	91519	1.85	9.85
C2	449	65122	624	90503	1.75	8.55
C3	460	66717	626	90794	1.80	10.81
C4	430	62395	635	92099	2.41	5.63
C5	435	63091	625	90649	2.37	8.01
C6	409	59320	620	89923	2.52	6.37
C7	419	60771	603	87458	2.49	8.34
C8	398	57725	592	85862	2.59	7.26
C9	411	59611	599	86878	2.52	7.19
C10	448	64977	646	93694	2.32	5.25
C11	434	62946	591	85717	2.38	8.74
C12	418	60626	615	89198	2.48	4.18
Average	**433**	**62767**	**618**	**89524**	**2.29**	**7.31**

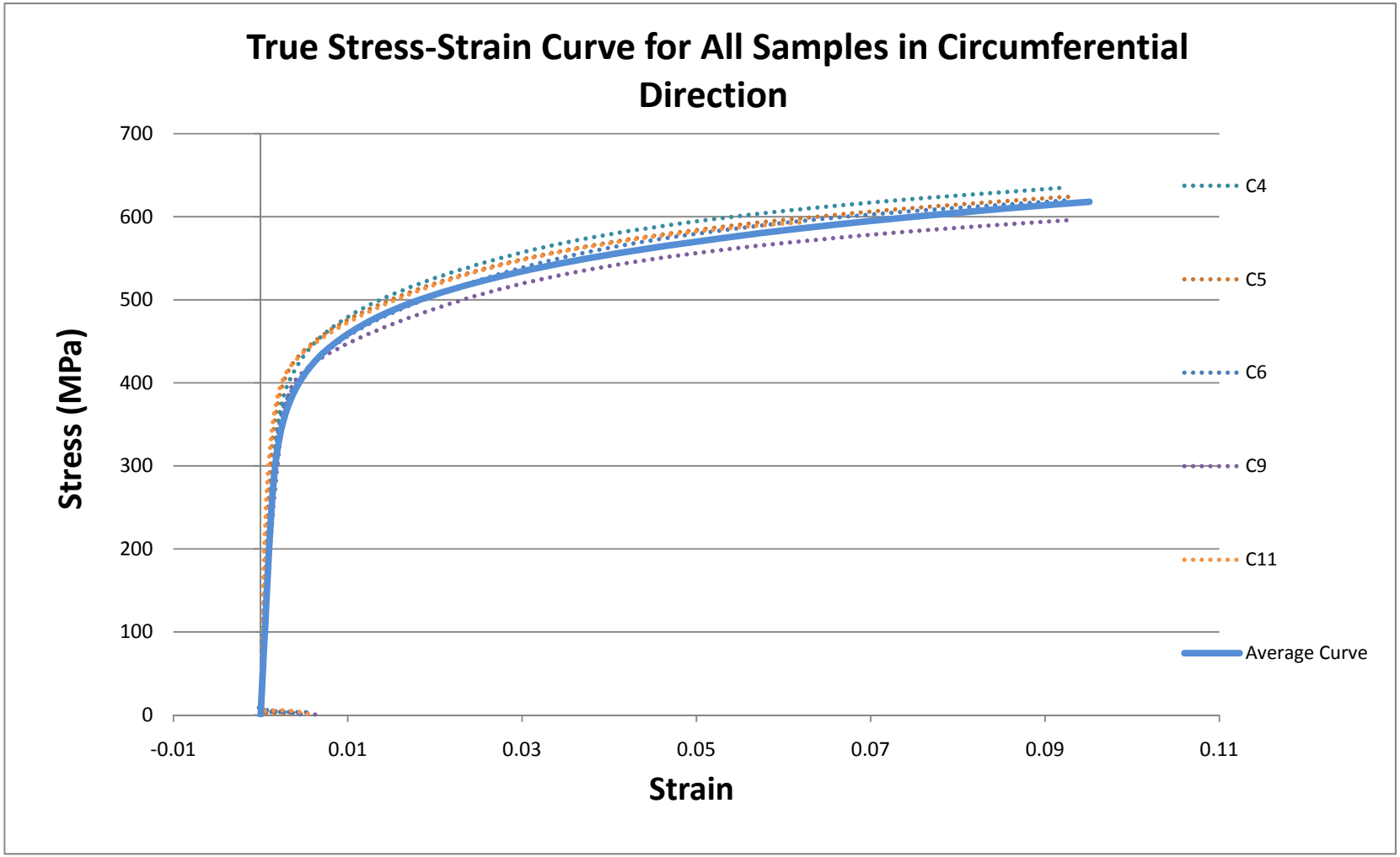

Figure 3.5- True Stress-Strain Curve for Some Samples in Circumferential Direction

3.1.2 Charpy Test

Before developing the recent methods for measuring the fracture toughness of materials, the Charpy test was traditionally used for evaluating material resistance to fracture. In the absence of fracture toughness data, CVN data can be correlated to fracture toughness. This test measures the energy absorption of a V-notched specimen while breaking under impact bending load.

The following factors affect Charpy impact energy:

❖ ***Temperature***

The greatest portion of the impact energy is absorbed by plastic deformation and by the yielding of the V-Notch during the test. Parameters, such as temperature, that affect the yield strength and ductility of the steel will affect the impact energy.

❖ ***Notch***

The notch radius and depth are very important for impact energy.

❖ ***Specimen Dimension***

According to ASTM E8M [20], the thickness of the full size specimens should be 10 mm. Since the thickness of the pipes does not allow testing full-size specimens; sub size specimens were used. The absorbed energy in sub-size specimens will be less than, that of the standard specimen. According to API 579 [1], there is no exact correlation between sub-size and full-size Charpy specimens for impact energy in pipeline materials. However, the following equations were suggested for upper shelf and lower shelf energies respectively by API 579 [1] for re scaling the impact energy to full-size specimens:

$$CVN_{US} = CVN_{US}^{S}\left(\frac{t_c}{t_c^S}\right)$$
$$CVN = CVN^{S}\left(\frac{t_c}{t_c^S}\right) \quad (3.4)$$

A set of 108 sub-size specimens were prepared from four different pipe sections and tested at eight different temperatures (-60,-40,-20, 3, 22, 50, 100 and 150 °C) in this study. 54 sub-size specimens, which were cut from 3 pipe sections, were tested at three different temperatures (50 ºC, 100 ºC and 150 ºC). The sub-size dimensions for flattened and non-flattened specimens are shown Figure 3.6. Figure 3.7 also shows a sample sub size specimen for Charpy test.

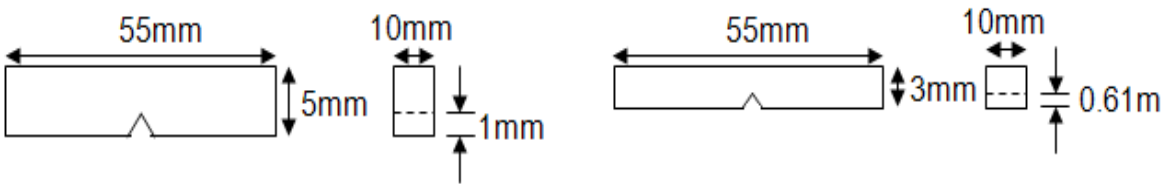

Figure 3.6- The Sub-Size specimen Dimensions for Charpy Test [20]

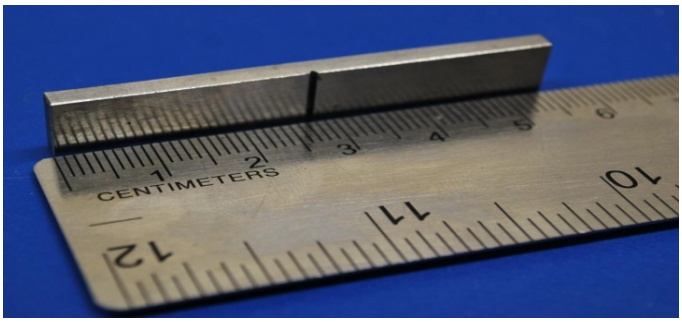

Figure 3.7- A Sample Sub Size Specimen for Charpy Test

The Charpy impact energies for tested specimens are summarized in Table 3.2.

Table 3.2- None Scaled Charpy Test Results [24]

	Average Energy E (J)		
Temperature (°C)	**t_c^s=3mm (Flattened)**	**t_c^s=3mm (Non-Flattened)**	**t_c^s=5mm (Flattened)**
150	N/A	11.0	26.0
100	12.0	12.0	25.0
50	N/A	11.0	24.0
22	14.0	13.0	19.0
3	12.0	9.0	16.0
-20	10.0	9.0	15.0
-40	8.0	8.0	7.0
-60	6.0	7.0	3.0

The results for the specimens scaled up to 10 mm thickness are shown in Figure 3.8 and Table 3.3, respectively. Note that in Figure 3.8, the data have scatter for two reasons: First, the 3mm and 5mm specimens were flattened which produced scatter in the results. Second, the scatter in the results was magnified on were scaling to the full specimen size.

It should be noted that Boltzmann function was used to produce the sigmoidal curve for the CVN test results. This function is shown in equation 3.5.

$$Energy = \frac{A1 - A2}{1 + e^{\frac{T-T0}{dx}}} + A2 \qquad 3.5)$$

Figure 3.8 shows that the transition temperature was approximately -22.9 ºC.

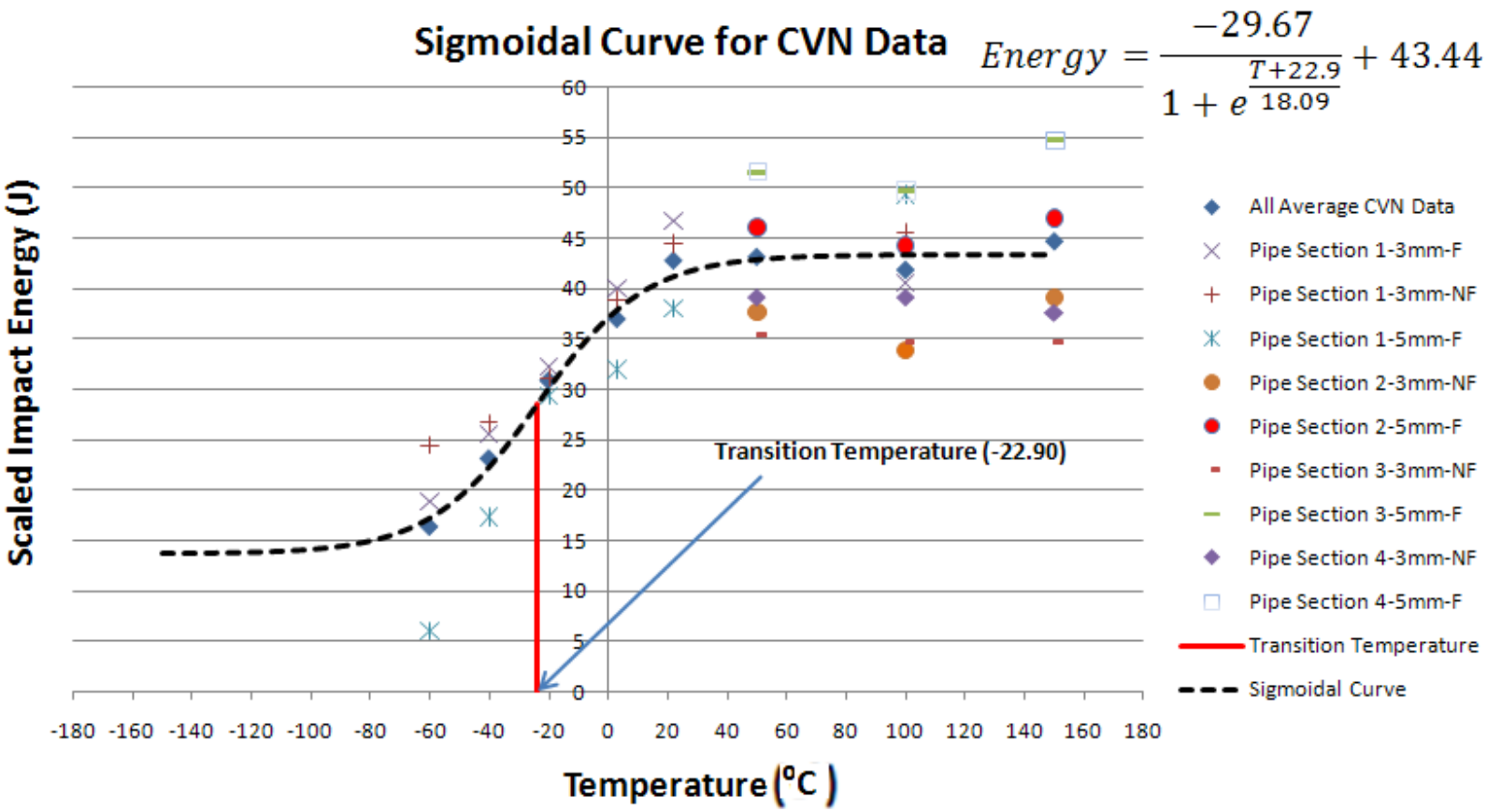

Figure 3.8- Scaled Energy Chart [24]

Table 3.3- Scaled Charpy Test Results [24]

	Average Energy E (J)		
Temperature (ºC)	**t_c^s=3mm (Flattened)**	**t_c^s=3mm (Non-Flattened)**	**t_c^s=5mm (Flattened)**
150	N/A	37.0	52.0
100	41.0	39.0	49.0
50	N/A	37.0	49.0
22	47.0	44.0	38.0
3	40.0	40.0	32.0
-20	32.0	31.0	29.0
-40	26.0	27.0	15.0
-60	19.0	24.0	6.0

Macroscopic observation was conducted to validate these results by capturing the shear fracture of the CVN specimens. Based on ASTM E23-07 [23], fully ductile fracture is indicated by 100% shear fracture, and the transition fracture is indicated by 50% shear fracture. The amount of shear in the CVN specimens is shown in Table 3.4 and Figure 3.9 respectively.

Table 3.4- The Shear Percentages of CVN Specimens [24]

Specimen Size (mm)	**t_c^s=5mm (Flattened)**	**t_c^s=3mm (Flattened)**	**t_c^s=3mm (Non-Flattened)**
Temperature (ºC)	**Percent Shear %**		
150	100.0	100.0	100.0
100	100.0	100.0	100.0
50	90.0	100.0	100.0
22	90.0	90.0	100.0
3	70.0	90.0	86.7
-20	50.0	80.0	46.7
-40	10.0	30.0	20.0
-60	0.0	0.0	10.0

$$Shear\ Percentage = \frac{-100.71}{1 + e^{\frac{T+22.9}{14.11}}} + 98.23$$

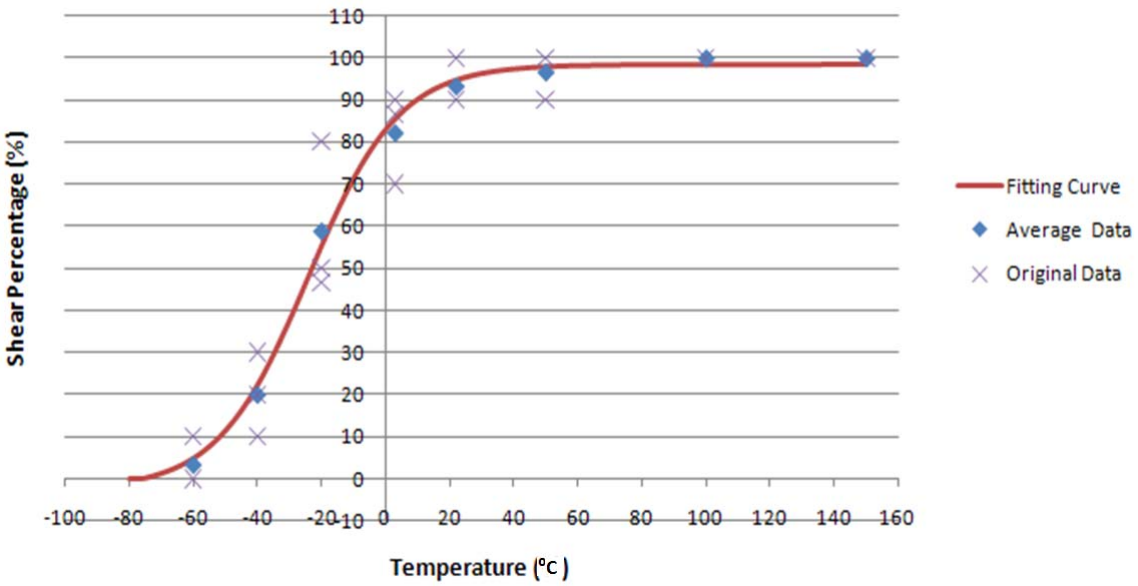

Figure 3.9- Shear Fracture Percentage Diagram [24]

Figure 3.9 shows that the 50% shear fracture occurs at -22.9 ºC which is in full agreement with the energy-temperature diagram (Figure 3.8) confirming that the transition temperature for the CVN specimens is -22.9 ºC. The results for the CVN test are summarized in Table 3.5.

Table 3.5- Summary of the Charpy Test Results [24]

Upper Shelf Average Energy E (J)	Lower Shelf Average Energy E (J)	Transition Temperature, DBTT (°C)	Average Shear Percentage (%) at -22.9 (ºC)
43.5	16.3	-22.9	50

The photomicrographies of the fractured surfaces at different temperature (ºC) are shown in Figure3. 10. The fracture surfaces showed that the type of fracture changed from brittle fracture at the low temperatures to ductile fracture at the higher temperatures.

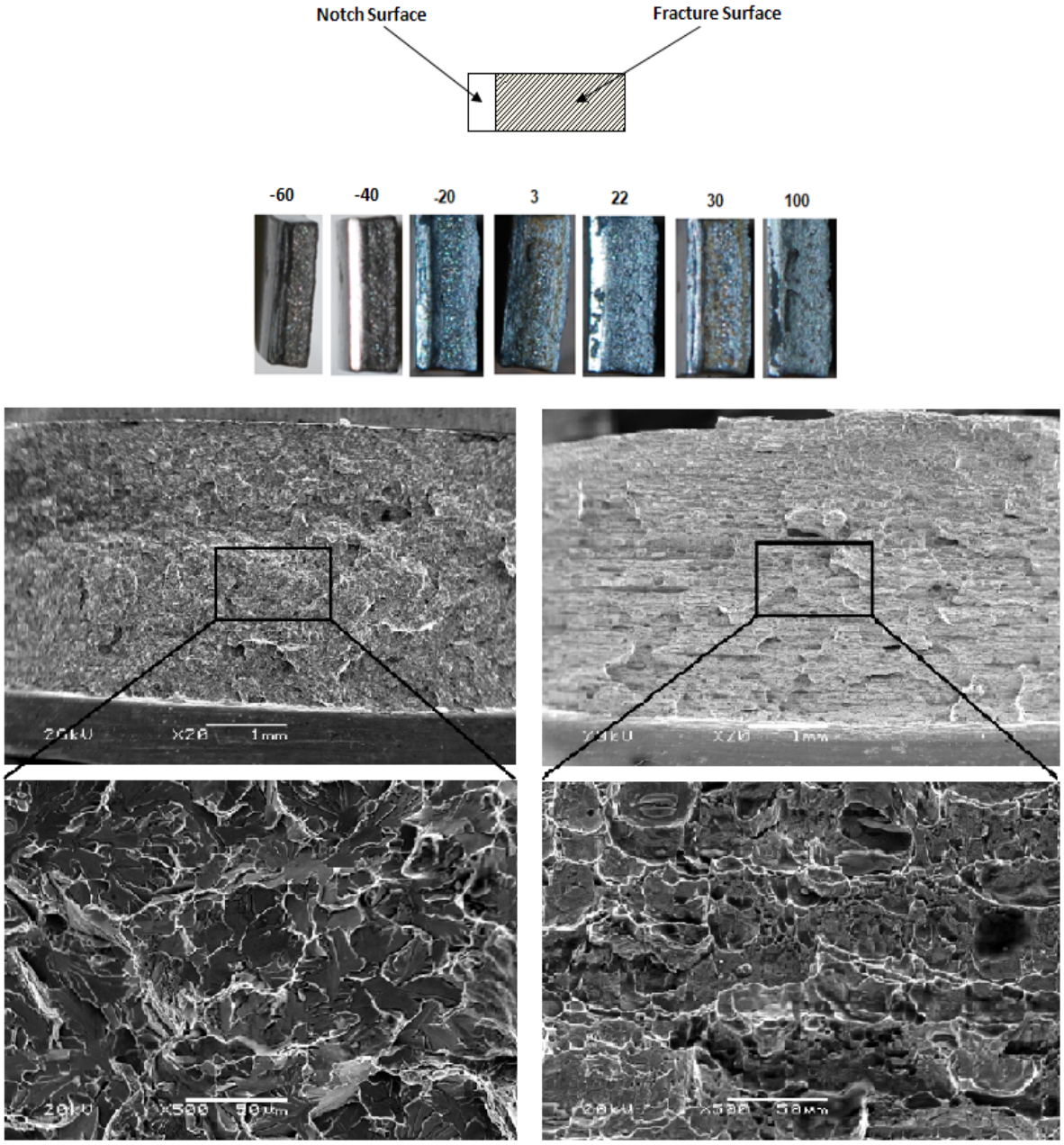

Figure3. 10- Fracture Surface of Specimens at Different Temperatures (ºC)

$K_{IC} - CVN\ Corrolation$

The following methods were studied in this work to correlate CVN impact upper bound to K_{IC}:

❖ ***API 579 [1]***

The following equation, which is known as the Rolfe-Novak equation [3], can be used for upper bound fracture toughness. It should be noted that this equation generally gives conservative results [3].

$$(\frac{K_{IC}}{\sigma_Y})^2 = 0.52(\frac{CVN}{\sigma_Y} - 0.02) \qquad (MPa\sqrt{m}\ ,\ J) \tag{3.6}$$

❖ ***CorLAS TM [17]***

This is a computer program for corrosion-life assessment of pressurized pipes and vessels [17]. The following empirical equation can be used for converting Charpy impact energy to J_c for upper bound values:

$$J_c = 10\ CVN \qquad (ft - lb)/(in^2) \tag{3.7}$$

Equation 3.7 produces a low value of fracture toughness.

❖ ***Tyson and CANMET***

Tyson (2005) proposed some relationships for converting CVN to K_{IC} [7]. A corresponding value of each curve at CVN=43.5 J was determined by drawing a vertical line at that point and determining the intersection of that line with each of the curves. This procedure is summarized in Figure 3.11. Figure 3.11 was digitized by Badr Bedairi [24].

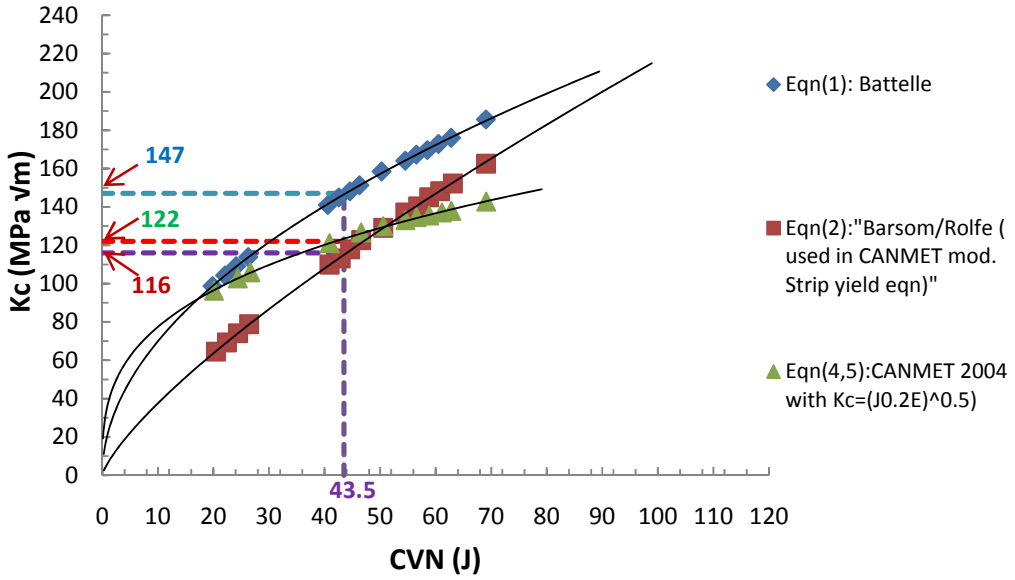

Figure 3.11- CVN vs. K_{IC} (Tyson 2005) [7]

❖ ***BS7910 [4]***

The following equation can be used for the lower bound of upper shelf fracture toughness. The equation 3.8 is plotted in Figure3.12.

$$K_{mat} = 17\ CVN + 1740 \tag{3.8}$$

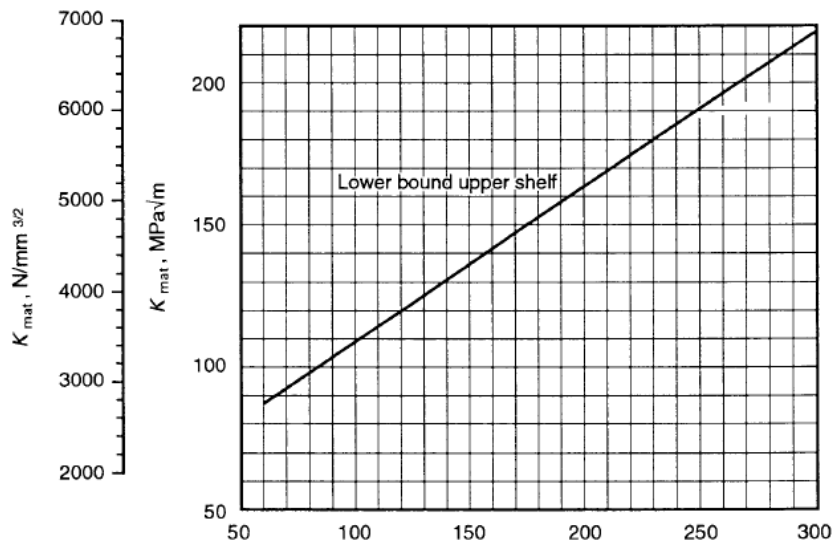

Figure3.12- K_{mat} Plotted against Charpy Impact Energy for Upper Shelf Behavior [4]

Table 3.6 summarizes the above methods for correlating Charpy impact energy to the fracture toughness.

Table 3.6- Charpy Impact Energy Correlation to Fracture Toughness in Different Methods

Methods	Charpy Upper Shelf Average Energy E (J)	Fracture Toughness ($MPa\sqrt{m}$)
API 579	43.5	89.0
CorLAS	43.5	108.0
Tyson & CANMET	43.5	128.0
BS 7910	43.5	80.0

4. Experimental Rupture Testing of Cracks, Artificial Corrosion and CIC Defects

To investigate the failure behavior of a pipe containing longitudinal long defects, a series of burst tests were carried out on end-capped, seam-welded pipe specimens. Three different types of defects of varying depths were created in pipes according to the test matrix (Table 4.1). The three types of defects are listed below:

- C: Artificial Corrosion
- Cr: Crack
- CIC: Crack in Corrosion

Table 4.1- Test Matrix

Defect Depth	Artificial Corrosion	Crack	Crack in Corrosion
(%WT)	**Length = 200 mm**	**Length = 200 mm**	**Length = 200 mm**
20	C1	CR1	CIC1
40	C2	CR2	CIC2
60	C3	CR3	CIC3

4.1 Artificial Corrosion Defects

According to the test matrix, artificial corrosion defects of varying depths were machined in a rectangular shape on the outside of the pipe. The corners of the rectangular pocket were rounded to avoid stress concentration (Figure 4.1 and Figure 4.2). The artificial corrosion length was 200 mm to be consistent with the other types of defect lengths such as crack and CIC defects. The crack defect length was chosen as 200 mm to increase the rate of crack propagation at the bottom of slit.

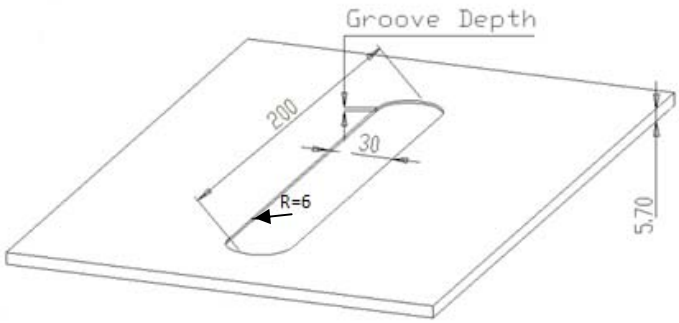

Figure 4.1- A Sample Corrosion Defect Profile [24]

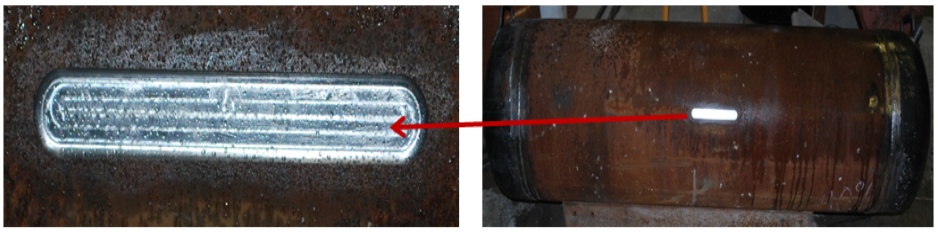

Figure 4.2- An Artificial Corrosion in a Tested Pipe

4.2 Crack Defects

To create a sharp crack based on the test matrix, a narrow slit was cut in the pipe and then the pipe was subjected to fatigue loading until a fatigue crack started to propagate at the bottom of the slit. The depth of the initial slit was varied, based on the required final defect depth. A sample slit defect and crack profile in a tested pipe after pre-fatiguing are shown in Figure 4.3 and Figure 4.4, respectively.

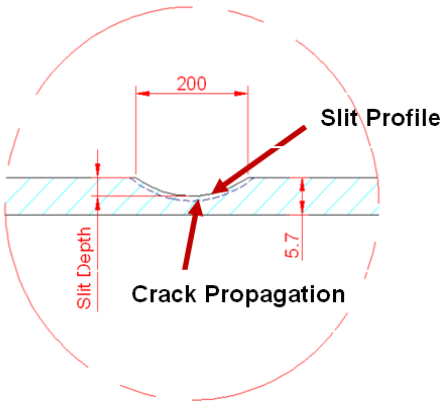

Figure 4.3- A Sample Slit Defect Profile

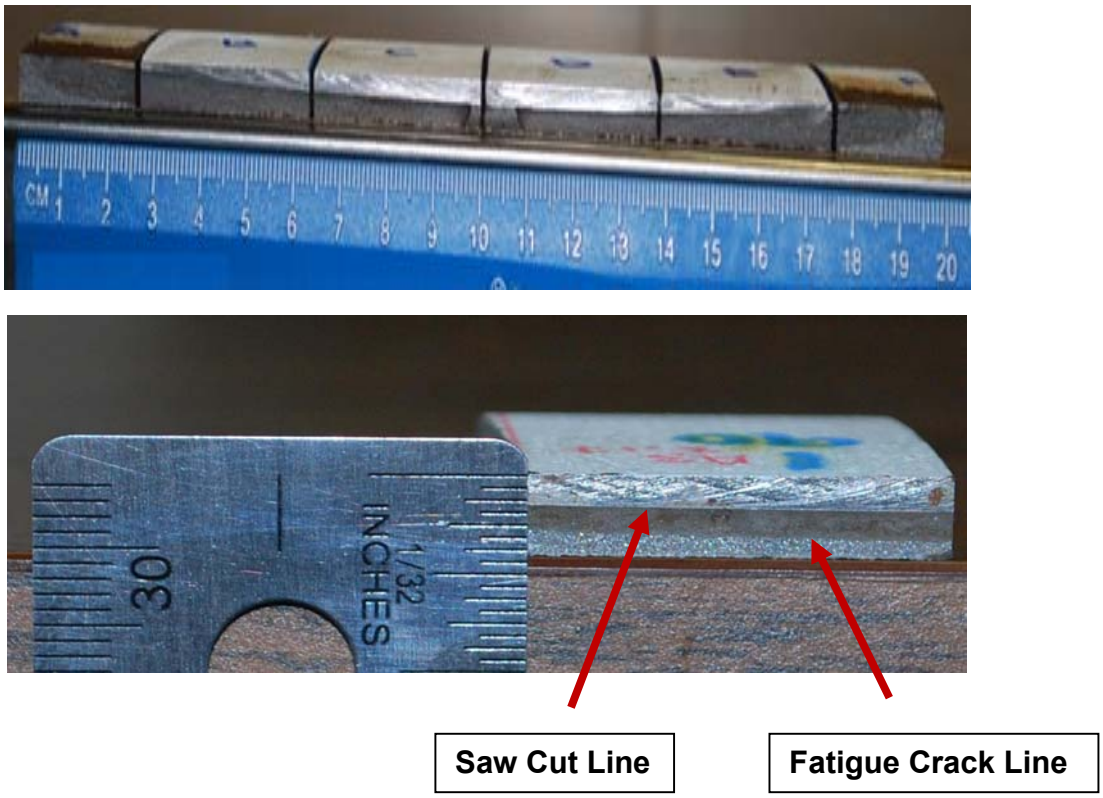

Figure 4.4- Crack Profile in a Tested Pipe after Pre-Fatiguing Procedure

Fatigue Test Machine

A servo-fatigue controller electro-hydraulic fatigue test machine, shown in Figure 4.5 , was used to pre-fatigue the pipes. The machine contents of a test frame and controller.

Figure 4.5- Fatigue Test Apparatus

Test frame is schematically shown in Figure 4.6.

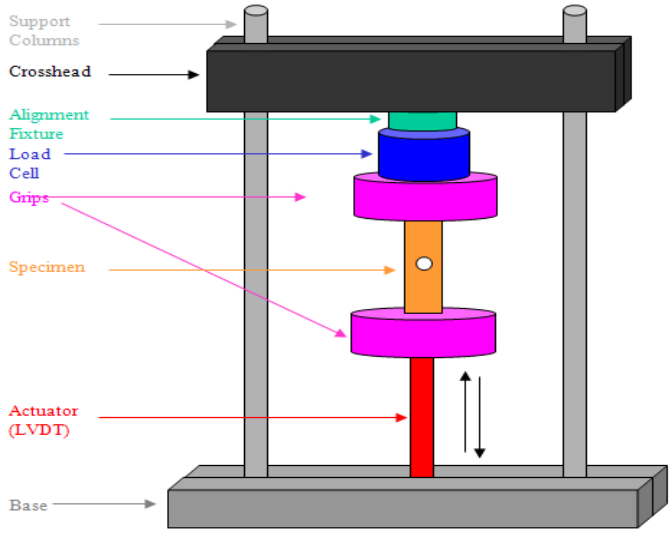

Figure 4.6- Components of the Test Frame [25]

This 406 controller is an electronic sub-system containing the principal servo control, failsafe and read out functions for one channel [27]. This controller is based on a ± 10 volt system. This means that all outputs, such as load, strain or displacement fall in the range.

In general, the output of the system is given in a percentage, i.e. +10 volts=100% or 2.5 volts =25% [27]. This is shown in Figure 4.7.

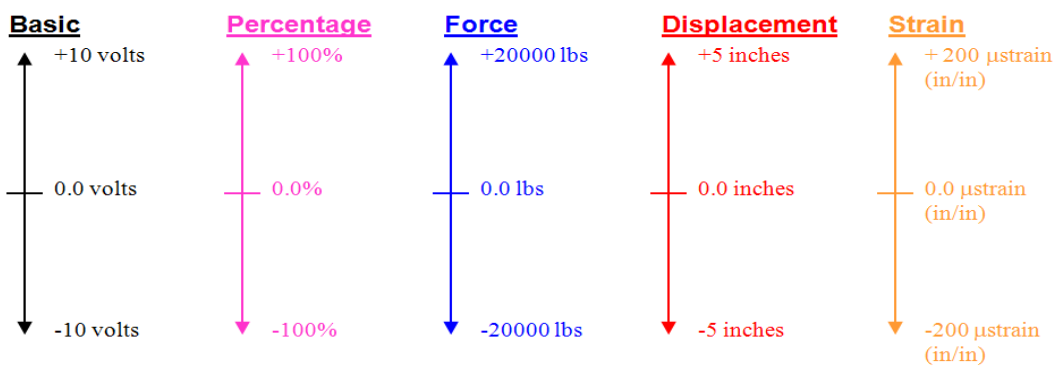

Figure 4.7-406 Controller Basics [25]

Loading Configuration [29]

In order to create a fatigue crack at the bottom of a slit, the pipe was cut into three pieces; each 600 mm long, for conserving material, convenience and due to the test set up limitations. After pre-fatiguing one of sections, two other pieces of the pipe were welded to the pre-fatigued section. The burst test was carried out after welding the end caps on these section pipes.

Creating the fatigue crack, the pipe was subjected to vertical cyclic load, which were applied by an actuator, and supported by upper grips (Figure 4.6). To avoid failure in the pipe, the maximum allowable load was calculated as follows:

The ring shown in Figure 4.8, is subjected to a line force, F, and supported by the ground. The elastic modulus and design stress of the material are E and σ_Y respectively.

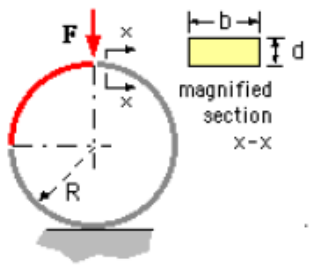

Figure 4.8- A Ring Which It Subjected to a Force [29]

Since the ring is symmetric, one quadrant of the ring is considered, and the free diagram of one quadrant of the ring is shown in Figure 4.9.

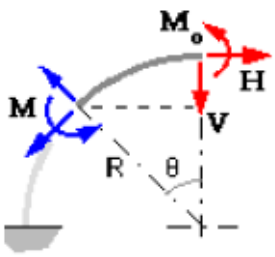

Figure 4.9- Free Diagram of One Quadrant of the Ring [29]

If there is no moment at the end of one quadrant of the ring then the end of the ring would rotate, but, as it is shown in Figure 4.10, the ring would not rotate because of the symmetry of the complete ring. There should be a moment (M) to ensure that the ring remains horizontal.

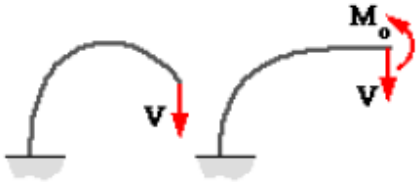

Figure 4.10- The Role of M_0 in the Ring [29]

In general, the shear and normal stress are insignificant in comparison to the bending stress for a long section beam. Therefore, for end equilibrium can be written as follows:

$$\sum M_{cut} \ at\ \theta = M + M_0 - VR\ sin\theta - HR\ (1 - cos\theta) = 0 \tag{4.1}$$

Therefore

$$M = -M_0 + VR\ sin\theta + HR\ (1 - cos\theta) \tag{4.2}$$

For H=0

$$M = -M_0 + VR\ sin\theta \tag{4.3}$$

According to Castigliano's theorem [30], equations 4.2 can be written as follows:

$$\frac{\partial M}{\partial V} = Rsin\theta$$

$$\frac{\partial M}{\partial H} = R(1 - cos\theta) \tag{4.4}$$

$$\frac{\partial M}{\partial M_0} = -1$$

For a curved beam in which bending strain is significant in comparison to shear and normal stress, the following equation can be written [30]:

$$\delta_G = \int length \frac{M}{EI} \frac{\partial M}{\partial G} \cdot ds \tag{4.5}$$

Where

G is an arbitrary load or moment which are applied on the system

The various deflection components with constant EI can be determined as below:

$$\delta_{M_0} = \frac{1}{EI}\int_0^L M \frac{\partial M}{\partial M_0}\, ds = \frac{1}{EI}\int_0^{\frac{\pi}{2}} (VR\, sin\theta - M_0)(-1)Rd\theta = \frac{R}{EI}(-VR + \frac{\pi}{2}M_0) \tag{4.6}$$

$$\delta_V = \frac{1}{EI}\int_0^L M \frac{\partial M}{\partial V}\, ds = \frac{1}{EI}\int_0^{\frac{\pi}{2}} (VR\, sin\theta - M_0)R^2\, sin\theta\, d\theta = \frac{R^2}{EI}(\frac{\pi}{4}VR - M_0) \tag{4.7}$$

$$\begin{aligned}\delta_H = \frac{1}{EI}\int_0^L M \frac{\partial M}{\partial V}\, ds &= \frac{1}{EI}\int_0^{\frac{\pi}{2}} (VR\, sin\theta - M_0)R(1 - cos\theta)R\, d\theta \\ &= \frac{R^2}{EI}[\frac{VR}{2} - \left(\frac{\pi}{2} - 1\right) M_0]\end{aligned} \tag{4.8}$$

As it was mentioned above, there is no end rotation, therefore, $\delta_{M_0} = 0$ and above equations can be expressed as:

$$M_0 = \frac{2VR}{\pi} \tag{4.9}$$

$$\delta_V = \frac{VR^3}{EI}(\frac{\pi}{4} - \frac{2}{\pi}) \tag{4.10}$$

$$\delta_H = \frac{VR^3}{EI}(\frac{2}{\pi} - \frac{1}{2}) \tag{4.11}$$

Since $V = \frac{F}{2}$ then for complete ring equations can be written as follows:

Side deflection (parallel to the external load)=$2\delta_V = \frac{VR^3}{EI}(\frac{\pi}{4} - \frac{2}{\pi})$ (4.12)

Side deflection (transverse to the external load)=$2\delta_H = \frac{VR^3}{EI}(\frac{2}{\pi} - \frac{1}{2})$ (4.13)

The maximum bending moment occurs at $\theta = 0$ based on equation 4.2. Therefore, the maximum bending moment is:

$$M_{Max} = M_0 = \frac{2VR}{\pi} \tag{4.14}$$

The significant stress is the bending stress, and the maximum bending stress becomes:

$$\sigma_{Max} = \frac{M_{Max} Y_{Max}}{I} = \frac{\left(\frac{2VR}{\pi}\right)\left(\frac{d}{2}\right)}{\frac{bd^3}{12}} = \frac{6FR}{b\pi d^2} \tag{4.15}$$

The maximum allowable load on the ring occurs when σ is equal to the yield stress; therefore, the maximum allowable load can be determined as below:

$$F_{Max} = \frac{b\pi d^2 \sigma_Y}{6R} \tag{4.16}$$

By using equation 4.16, the maximum load becomes 17400 N. This load is the maximum load for yielding in the pipe; therefore, a lower load was used for pre-fatiguing the pipes (13350 N).

By using the above equations, the bending stress was calculated at $\theta = 0$ and $\theta = 90$ respectively. Furthermore, the angle was determined where the bending stress is zero, was also determined. The specification of the pipe and a summary of the analytical and finite element results in a pipe under cyclic loading are summarized in and Table 4.2 and Table 4.3 respectively. The small difference between the finite element and analytical results may be due to some simplified assumptions which were made in the analytical approach.

Table 4.2- The Specification of the Pipe under Cyclic Loading

Pipe Length (mm)	Pipe Thickness (mm)	Pipe Radius (mm)	Applied Load (N)
600	5.7	254	13350

Table 4.3- A Summary of the Analytical and Finite Element Results in a Pipe under Cyclic Loading

Angle (Degree)	Analytical Results			Finite Element Results			Experimental Measurement (mm)
	Side Deflection (mm)	Vertical Deflection (mm)	Hoop Stress (MPa)	Side Deflection (mm)	Vertical Deflection (mm)	Hoop Stress (MPa)	
$\boldsymbol{\theta = 0}$ (Top)	N/A	8.80	322	N/A	7.90	338	8.3
$\boldsymbol{\theta = 90°}$ (Side)	7.80	N/A	189	6.35	N/A	155	7.1
$\boldsymbol{\theta = 39.54°}$ (Minimum)	N/A	N/A	0	N/A	N/A	N/A	N/A

Crack Propagation [31],[32]

The remaining life of cracked component can be calculated using the relationship between cyclic crack growth rate $\frac{da}{dN}$ and stress intensity range ΔK given by (equation 4.17) according to Paris and Erdogan [32].

$$\frac{da}{dN} = c\,(\Delta K)^m \tag{4.17}$$

This equation has some limitations at the lowest and highest growth rates; the curve becomes very steep approaching a vertical asymptote. The asymptote at the lowest and highest growth rates are $K_{th}\ and\ K_c$ respectively. This quantity is explained as a lower limiting value of ΔK , which is known as the fatigue threshold stress intensity range, below which crack growth does not occur. At the very high growth rates, the curve becomes nearly vertical due to rapid unstable crack growth before final fracture occurs. This is shown in Figure 4.11.

To calculate the C and m, constants in equation 4.17, the log (da/dN) vs. the log (ΔK) for pipes tested are plotted. But, as it is shown in Figure 4.12, the results were variable and the average values corresponding those tests for C and m were 2.0×10^{-6} and 0.84 respectively; hence, the determined values for C and m were not true and couldn't use to predict crack propagation after specific number of cycles. This is interpreted due to the variation in the slit length and depth and limitation of the numbers of test which were done in this study.

The required number of cycles for creating a fatigue crack at the bottom of slit was varied between 75000 to 150000 cycles for different tests. It is worth noting that the crack propagation in a semi-elliptical crack depends on the stress intensity at the surface and the bottom of the slit. The variation in the slit length and depth cause the variation in the stress intensity in the surface and the bottom of the slit in different tests. Therefore, the crack propagation after specific number of cycles was predicted based on Magnetic particle, experience, NDT measurement and observation.

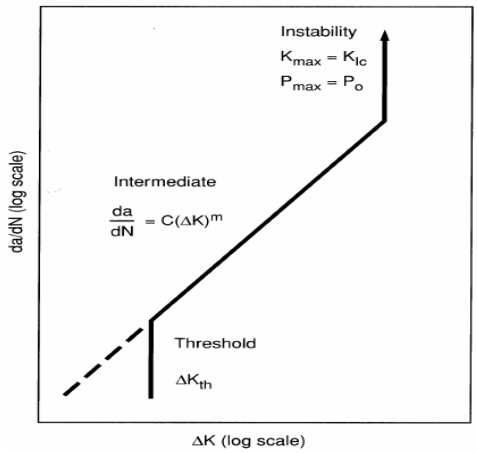

Figure 4.11- Variation of Fatigue Crack Growth Rates ($\frac{da}{dN}$) and Stress Intensity Range (ΔK) [14]

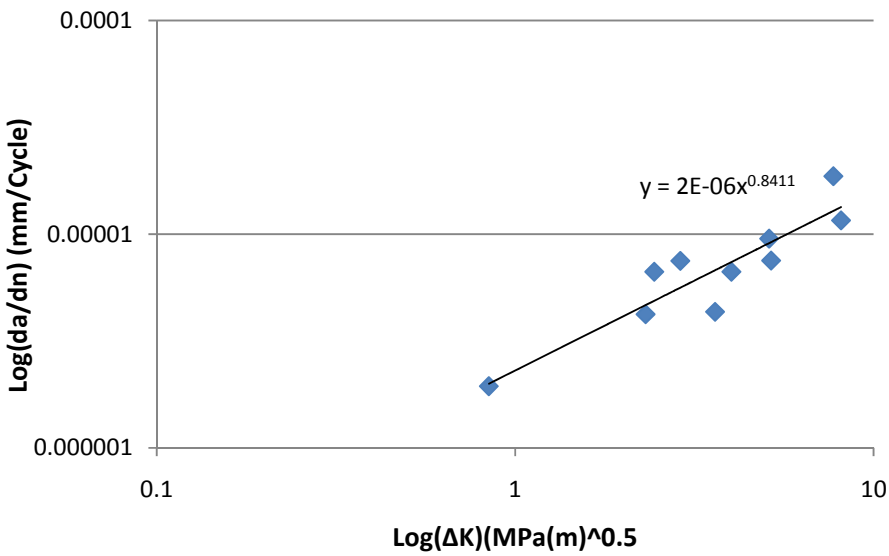

Figure 4.12- Crack Growth Rates vs. Stress Intensity Range

Crack Detection Techniques

One of the most widely used methods to detect the small crack growth is potential drop. However, it has been shown that the potential drop method is not very accurate for measuring the small crack growth [33]. The Magnetic particle testing method consists of establishing a magnetic field in the specimen, applying magnetic particles to the surface of the part, and examining the surface for accumulations of these particles that indicate discontinuities. A magnet will attract magnetic particles to its ends or poles, as they are called. Magnetic lines of force or flux flow between the poles of a magnet. Magnets will attract magnetic materials only where the lines of force enter and leave the magnet at the poles. If a magnet is bent and the two poles are joined so as to form a closed loop, no external poles will exist and consequently it will have no attraction for magnetic material. As long as the part has no cracks or other discontinuities, magnetic particles will not be attracted. When a crack or other discontinuity is present in the part being tested, north and south magnetic poles are set up at the edge of the discontinuity [36].

This method was used in the present study because it is safe, fast, easy, sensitive low cost way to find small cracks. It is important to ensure that parts are thoroughly cleaned and dried before conducting magnetic particle inspection. All surfaces to be inspected should be free of contaminants, paint, and other coatings that could prevent magnetic particle from entering the discontinuities. The procedure is shown in Figure 4.13 and Figure 4. 14.

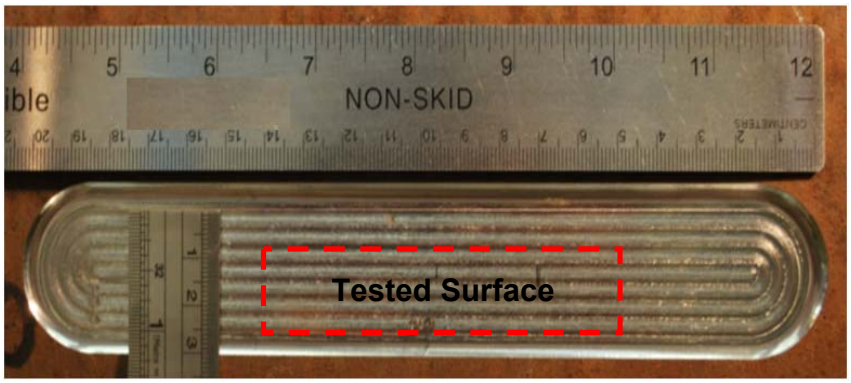

Figure 4.13- Surface Containing a Crack for a CIC Defect in a Pipe Tested Prior Detecting the Crack

The procedure was as follows:

First, the cleaner spray was used to clean and remove any contaminant from defect surface. As shown in Figure 4.13, there is no obvious indication of crack on the defect surface. After applying the magnetic particle and developer the crack was detected as shown in Figure 4. 14. This method was used successfully for the crack locating.

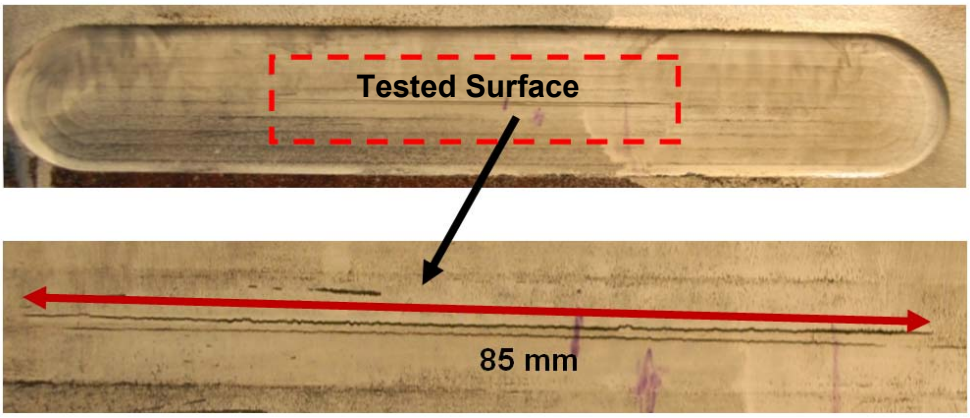

Figure 4. 14- Surface Containing a Crack for a CIC Defect in a Tested Pipe after Detecting the Crack

4.3 Crack in Corrosion (CIC) Defects

To create a crack in corrosion (CIC) defect a narrow slit was first machined in the pipe. The pipe was then cycled until a fatigue crack started to propagate from the bottom of the slit. Following this, an artificial corrosion (groove) to duplicate a defect was machined as a rectangular shape over the initial narrow slit on the outside of the pipe. The corners of the rectangular pocket were rounded to avoid stress concentrations. The depth of the corrosion defect was the same as the depth of initial slit. A schematic of the CIC defect is shown in Figure 4.15. The stepwise procedure for forming the CIC defect is shown in Figure 4.16.

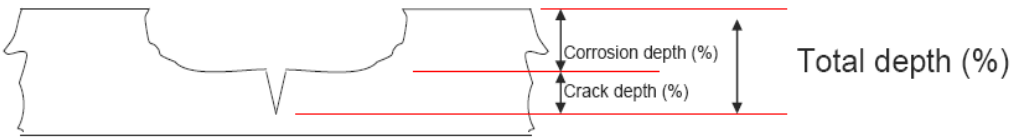

Figure 4.15- Transverse view through CIC flaw and definition of depth [6]

Step 1:

Machining Initial Slit

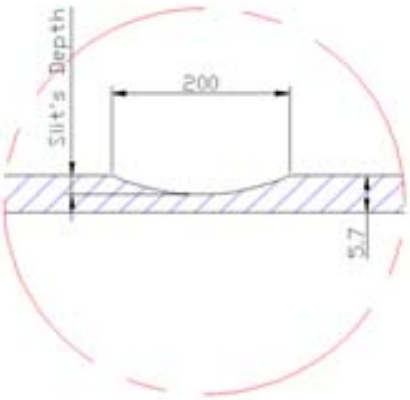

Step 2:

Pre-Fatiguing the Pipe

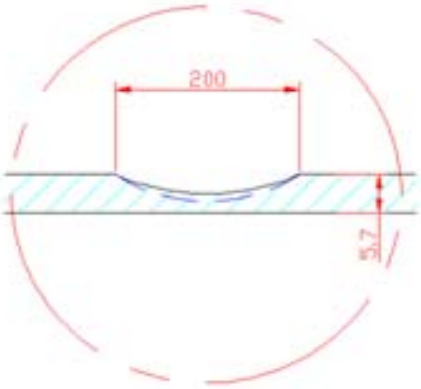

Step 3:

Machining Corrosion

Defect on the Initial Slit

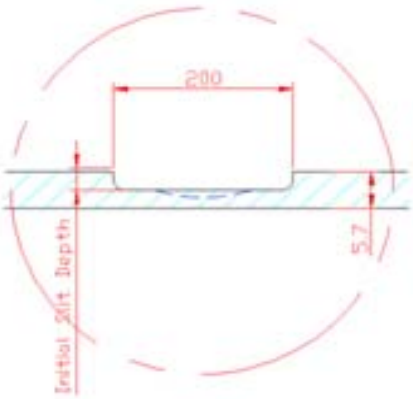

Figure 4.16- The Creation Procedure of a Crack in Corrosion Defect

4.3.1 Burst Test Procedure [11]

The following steps were used for the pipe burst tests:

- **Defect measurement-** All defects on the pipes were accurately measured for the length, width and location.
- **Pipe Dimensions-** The pipe wall thickness and diameter were measured in four locations in each pipe.
- **Defect Photographs-** All defects were photographed in color
- **Burst Testing-** All pipes were closed with hemispherical end caps and filled with water. The pipe was first pressurized to 1 MPa and, inspected for leaks. The pressure was then increased at a rate of $9.83 \times 10^{-5}\ m^3/min$ until failure occurred. The internal pressure in the pipe was continuously measured using a pressure transducer and amplifier.
- **Failure Photographs-** The failure location was photographed and the initiation site was identified. The initiation site could be determined based on localized necking through the wall thickness, bulging of the pipe material and the fracture surface. A rupture sample is shown in Figure 4.17.

Figure 4.17- Sample Tested Pipe after Running the Burst Test

5. Results and Discussion

Full-scale burst tests were undertaken to investigate the failure behavior of crack, corrosion and crack in corrosion defects. Initially, the failure behavior of corrosion and crack defects was investigated separately. These defects were then combined to evaluate changes in behavior based on the relative depth of the crack in the corrosion [7].

5.1 Artificial Corrosion Defect Rupture Tests

Three successful burst tests with different defect depths were completed to study the failure behavior of artificial corrosion defects in pipelines. Three long and axial uniform grooves of varying depths were machined to simulate corrosion defects in pipelines (Figure 4.1). The geometry and experimental failure pressures of the three pipes tested are summarized in Table 5.1.

Table 5.1- Geometry and Test Results

Test ID	Pipe Dimension (mm)			Defect Dimension (mm)			Experimental Failure Pressure (MPa)
	L	D	t	L (2c)	Width (mm)	Depth (a) (%WT)	
C1	1800	508	5.7	200	30	22	12.8
C2	1800	508	5.7	200	30	45	9.59
C3	1800	508	5.7	200	30	61	6.00

Failure Pressure Prediction-Modified B31G and RSTRENG

The predicted failure pressures of the pipes tested were calculated based on Modified B31G and RSTRENG. The results are given in Table 5.2 and shown in Figure 5.1. The RSTRENG method provided conservative results between 8% and 26% of the experimental values (with an average error of 20%). The Modified B31G also provided conservative results for the shallower defects (22% and 45% WT) between 14% and 24% of the experimental results, however, for the deeper defect (60% WT) the results was non conservative -9% of the experimental value.

The results show that RSTRENG was a more reliable method than Modified B31G. RSTRENG uses a more complete description of the longitudinal geometry of the real corrosion defect in comparison with Modified B31G.

Table 5.2- The Geometry and the Comparison between the Predicted and the Experimental Failure pressures of Pipes Tested

Test ID	Experimental Failure Pressure (MPa)	Predicted Burst Pressure		$Error(\%) = \frac{Experimental - Predicted}{Experimental} \times 100$	
		RSTRENG (MPa)	MB31G (MPa)	RSTRENG	MB31G
C1	12.8	9.47	9.73	26.0	24.0
C2	9.59	7.10	8.25	26.0	14.0
C3	6.00	5.51	6.54	8.0	-9.0
		Average Error (%)		**20.0**	**10.0**

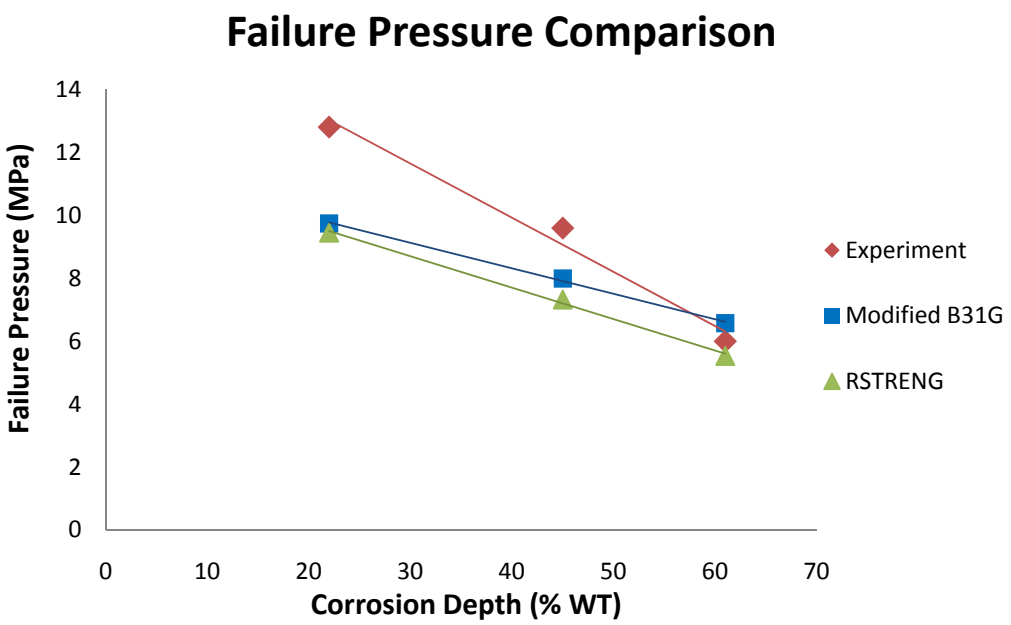

Figure 5.1- Failure Pressures Comparison between the Analytical Methods and the Experimental

The longitudinal length of a corroded area is the most important parameter for determining the failure pressure. The circumferential size has a smaller influence on the failure pressure. However, in this study, the only difference between these tests was of varying depth of grooves.

The failure of the artificial corroded pipes occurred due to plastic collapse by ductile tearing. This is verified by examining the fracture surfaces of pipes tested. As discussed in Chapter 2, the failure criterion, used in both RSTRENG and Modified B31G, predicts the onset of ductile tearing at a critical point within the corrosion defect. Plastic collapse of a corrosion defect occurs by local necking of the ligament by increasing the hoop stress. This occurs by increasing pipe radius and decreasing the wall thickness and the hoop stress overcomes the material strain hardening.

Figure 5.2 shows one of the corroded tested pipes (61% WT) after the burst test.

Figure 5.2- The Artificial Corroded Pipe (61% WT) after the Burst Test

5.2 Crack Defect Rupture Tests

A series of full-scale rupture tests were undertaken on the end-capped and seam-welded pipe specimens to investigate the failure behavior of axial crack-like flaws. Four burst tests were completed on specimens with similar defect lengths and varying depths. The pipes contained a semi-elliptical crack, shown schematically in Figure 5.3. The crack geometries and experimental collapse pressures of these pipes are provided in Table 5.3.

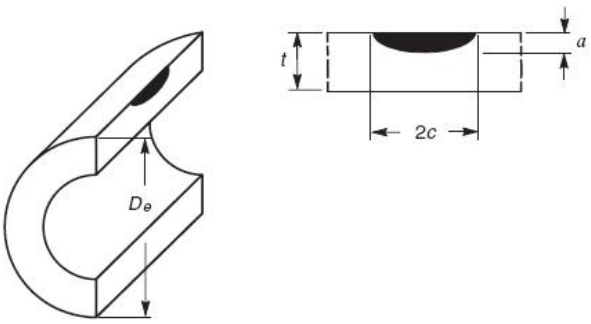

Figure 5.3- A pipe under internal pressure containing a semi-elliptical crack

Table 5.3- Geometry of tested pipes for Crack Defects

Test ID	Pipe Dimension (mm)			Defect Dimension (mm)		Experimental Failure Pressure (MPa)
	Length	Diameter	Thickness	Length (2c)	Depth (a) (%WT)	
CR1	1800	508	5.7	200	38%	10.1
CR2	1800	508	5.7	200	47%	9.30
CR3	1800	508	5.7	200	48%	9.60
CR4	1800	508	5.7	200	51%	8.83

Failure Pressure Prediction

The integrity analyses compared the burst predictions based on level 2 and level 3 FAD using BS7910 and API 579. To provide a consistent basis of comparison, the safety factors for the flaw dimensions, acting stresses and fracture

toughness values were set to unity. The results were then compared with the CorLAS and NG-18 methods. The stress intensity and reference stress solutions based upon API 579 and BS 7910 used in this study are given in Appendix A and B.

API 579 and BS7910 Using Level 2 and Level 3 FAD

Level 2 and level 3 FAD for both API 579 and BS7910 cylinder approaches for the pipes tested are shown in Figure 5.4 where that the BS 7910 cylinder approach is more conservative than the API 579 cylinder approach.

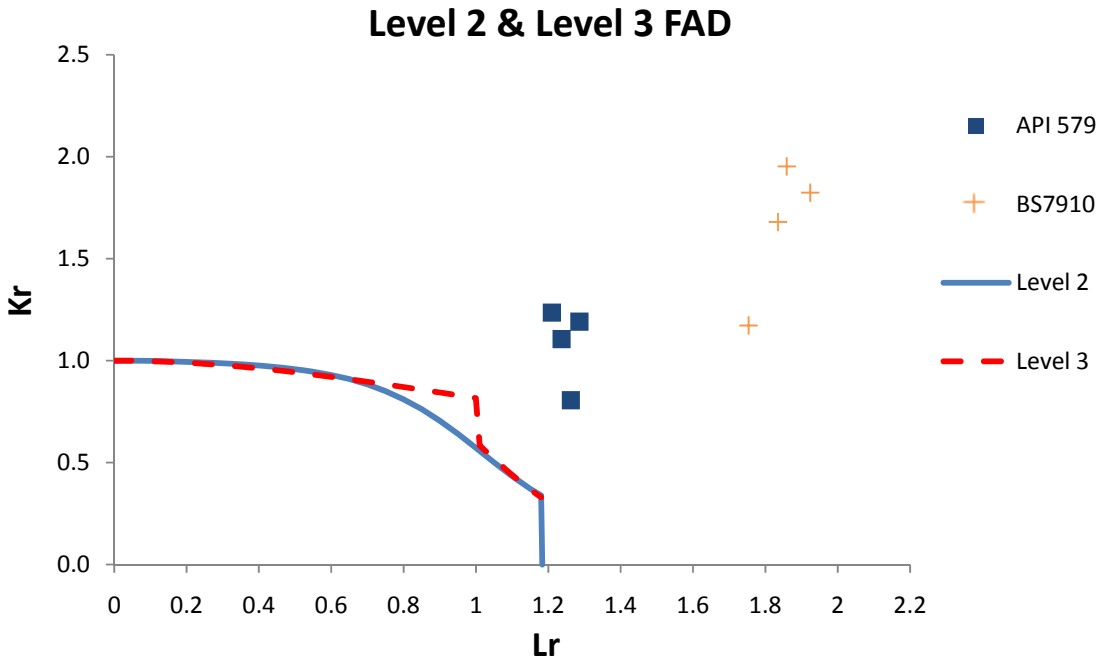

Figure 5.4- Assessment of the Failures Using Level 2 and Level 3 FAD for Two Different Approaches for Pipes Tested

The FAD is based on the relationship between fracture toughness ratio and load ratios. An increase in load or crack size moves the assessment point (k_r, L_r) along loading path towards the failure line as shown inFigure 5.5. As shown in Figure 5.5, the FAD curve is divided into three regions. The first of these regions is small-scale yielding, the second contains yielding and the last, plastic collapse [16].

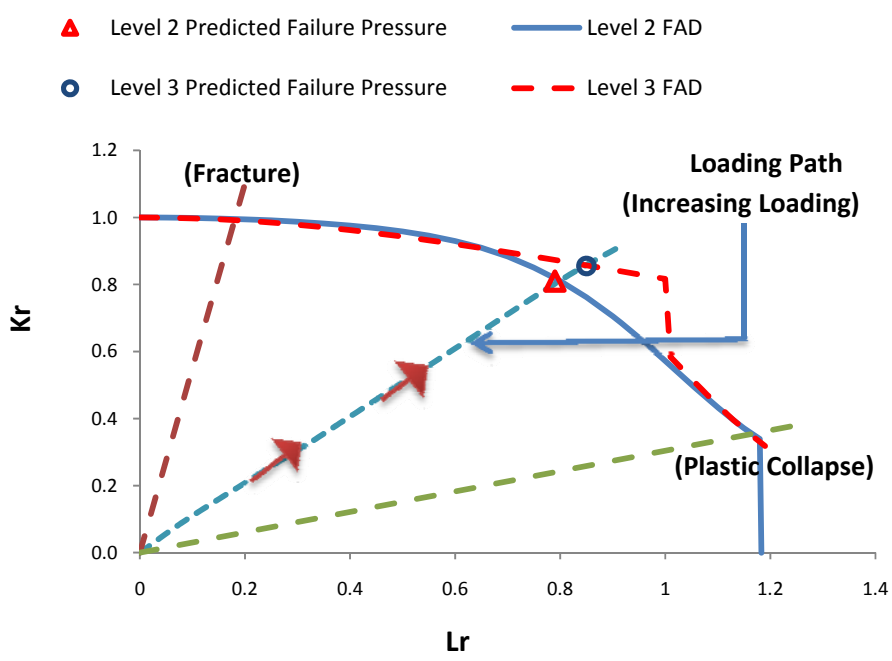

Figure 5.5- Failure Assessment Diagram (Loading Path)

To predict the failure pressure of the pipe sections with varying crack depths, a loading path for each crack configuration is constructed on the K_r vs. L_r plot. The intersection of the loading path with the failure lines (Level 2 & Level 3 FAD) defines the predicted failure pressures.

As indicated in Figure 5.5, the predicted failure pressures based on level 2 and level 3 FAD are different. Level 2 FAD is the normal assessment line (Equation 2.7) for general applications based on limited ductile tearing. The level 2 FAD is independent of the material true stress-strain curve and only uses the yield and tensile strength of the material. Level 3 FAD uses the true stress-strain curve of the material and it is unique for each material. Level 3 FAD is used when a full analysis of ductile tearing is available. Therefore, level 3 FAD was used in this study for both API 579 and BS 7910 approaches in order to predict the failure pressure of pipes tested. Figure 5.6 displays the FAD curves (level 2 and 3) and analytical predictions applying API 579 cylinder. Figure 5.5 and Figure 5.6 show that $L_r^{max} = 1.18$ corresponds to the cut-off value for the material properties of the pipes tested.

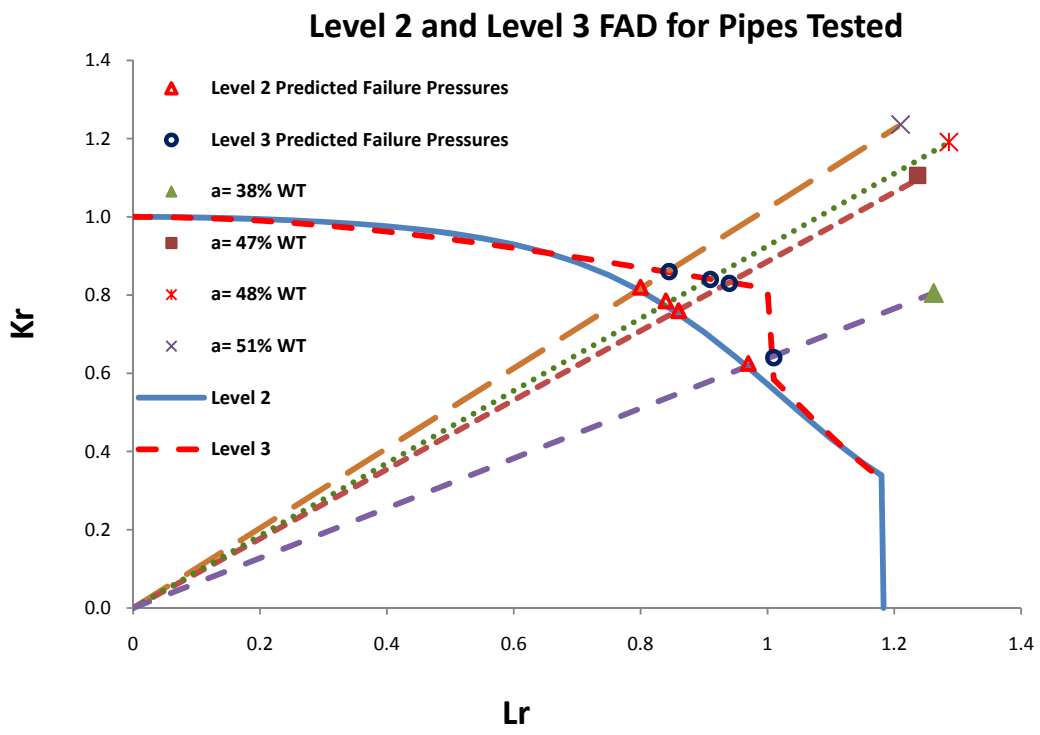

Figure 5.6- The Predicted Failure Pressures of Tested Pipes Based on API 579 Level 2 & 3 FAD (Cylinder Approach)

Level 3 FAD cylinder approach with the API 579 procedure provided conservative results between 20% and 30% of the experimental results (average error of 25%), whereas the level 3 FAD with BS 7910 given lower that were between 43% and 55% (average error of 50%) of the experimental failure pressures.

NG-18 Failure Criterion

The NG-18 criterion also provided conservative results between 30% and 33% of the experimental results (with an average error of 33%) given in Table 5.4.

CorLAS

CorLAS provided the least conservative results between 16% and 21% of the experimental results (with an average error of 18%). Figure 5.7 shows a semi-elliptical crack profile for CR4 specimen (51%WT) using CorLAS with the same length and effective area as the worst effective flaw.

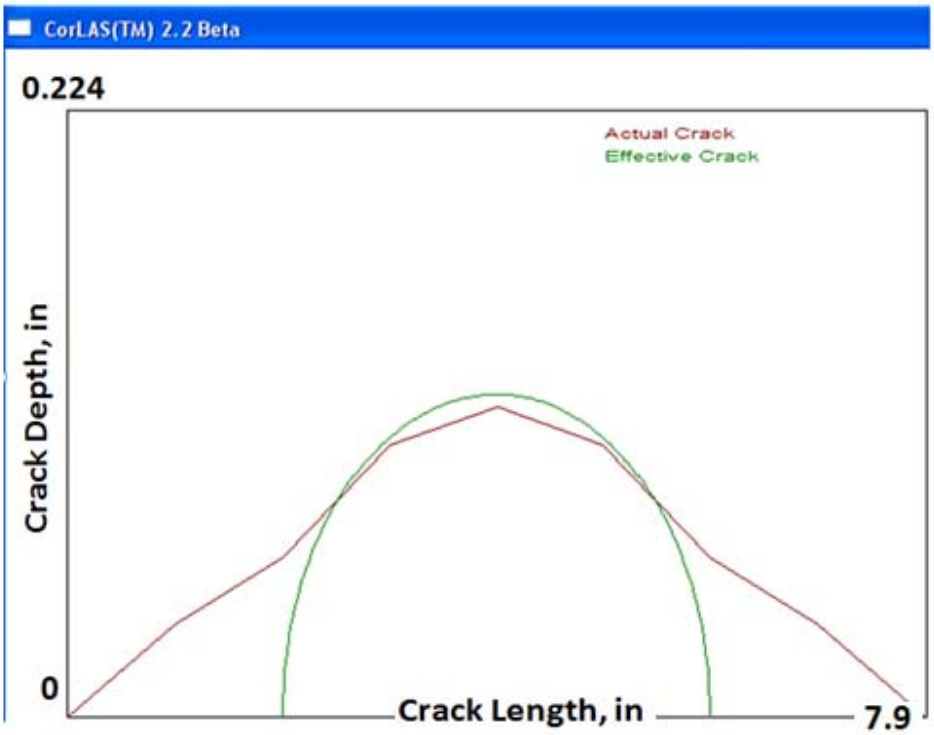

Figure 5.7- Crack Profile for CR4 pipe (51%WT) Using CorLAS

The results obtained by the above methods are summarized in Table 5.4 and Figure 5.8. All methods predicted a failure pressure less than the experimental failure pressure. The CorLAS results gave very good agreement with the experimental results. The most conservative predictions were made using BS7910 Level 3 FAD.

Table 5.4- Comparison of Measured and Predicted Failure Pressures for the Pipes Tested in Different Methods

Test ID	Crack Depth (a) (%WT)	Experimental Failure Pressure (MPa)	Predicted Failure Pressure (MPa)				$Error(\%) = \frac{Exp. - Pred.}{Exp.} \times 100$			
			API 579 Cylinder	BS7910 Cylinder	CorLAS	NG-18	API 579 Cylinder	BS7910 Cylinder	CorLAS	NG-18
CR1	**38**	10.1	8.10	5.80	8.48	7.10	20.0	43.0	16.0	30.0
CR2	**47**	9.30	7.10	4.62	7.69	6.30	24.0	50.0	17.0	32.0
CR3	**48**	9.60	6.86	4.45	7.58	6.20	29.0	54.0	21.0	35.0
CR4	**51**	8.83	6.21	3.97	7.24	5.90	30.0	55.0	18.0	33.0
				Average Error (%)			**25.0**	**50.0**	**18.0**	**33.0**

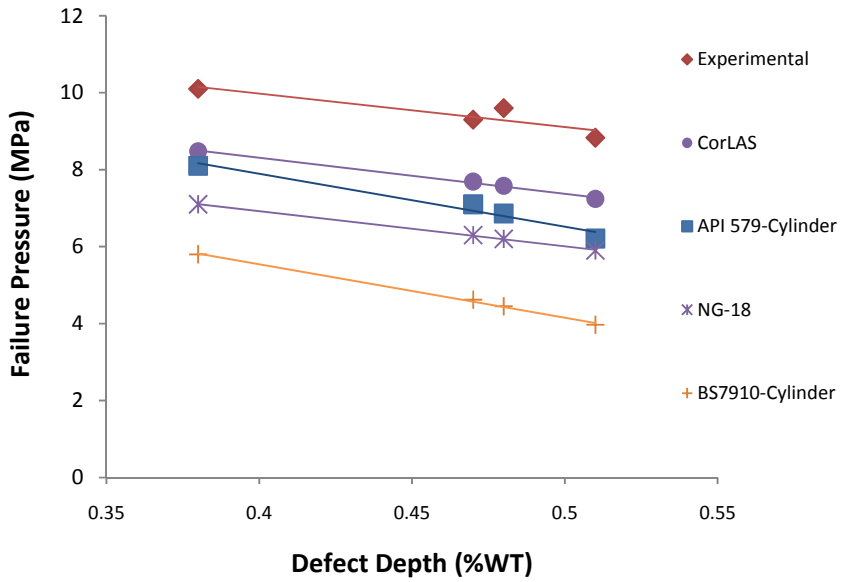

Figure 5.8- Comparison of Measured and Predicted Failure Pressures for the Pipes Tested

The BS7910 level 3 FAD was more conservative than the API 579 level 3 FAD for cylinders because of the applied stress intensity factor and reference stress solution. The API 579 level 3 FAD uses the bulging factor (M) directly in the stress intensity factor solution (Annex B). Whereas, BS7910 level 3 FAD determines the stress intensity based on the flat plate equation and the multiple bulging factor (M) to address bulging. The reference stress is calculated based on the flat plate equation in both methods. The calculated reference stress in BS 7910 is greater than that of API 579 because the bulging factor in BS 7910 is multiplied by 1.2 (Annex A).

According to Figure 5.5 and a review of the results in Figure 5.6, failures for all crack defects (38%, 47%, 48% and 51% WT) were expected to occur by plastic collapse, verified by examining the fracture surfaces. Ductile tearing occurs due to a process of void nucleation and growth. In some cases the failure collapse occurs because of a combination of ductile tearing and plastic collapse. The failure could be initiated due to plastic collapse and continue with ductile tearing or vice versa.

Figure 5.9 shows an overall micrograph of the fracture surface containing fatigue and ductile regions in CR4. Figure 5.10shows more detail of the initial

fatigue crack and Figure 5.11 shows the final ductile surface following the rupture test.

The NG-18 equation has been used widely because it is relatively simple and requires a limited amount of material property data. It is generally considered as a conservative method although the degree of conservatism depends on the crack size and material property.The value for fracture toughness in the NG-18 equation was calculated based on the upper shelf Charpy impact energy using equation 2.15 and was about two or three times greater than the actual fracture toughness of the same material. Therefore, the predicted failure pressure would be expected to be considerably higher than the experimental collapse pressure.

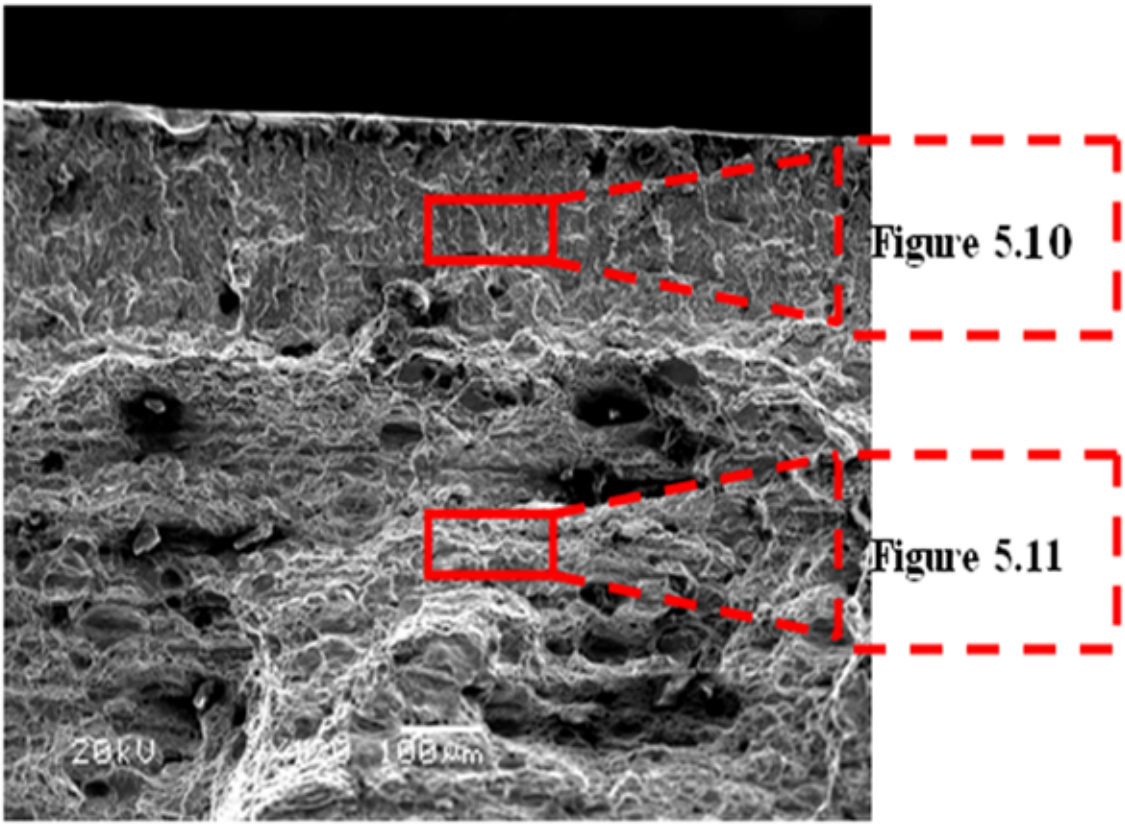

Figure 5.9- Fatigue Surface and Ductile Failure Surface

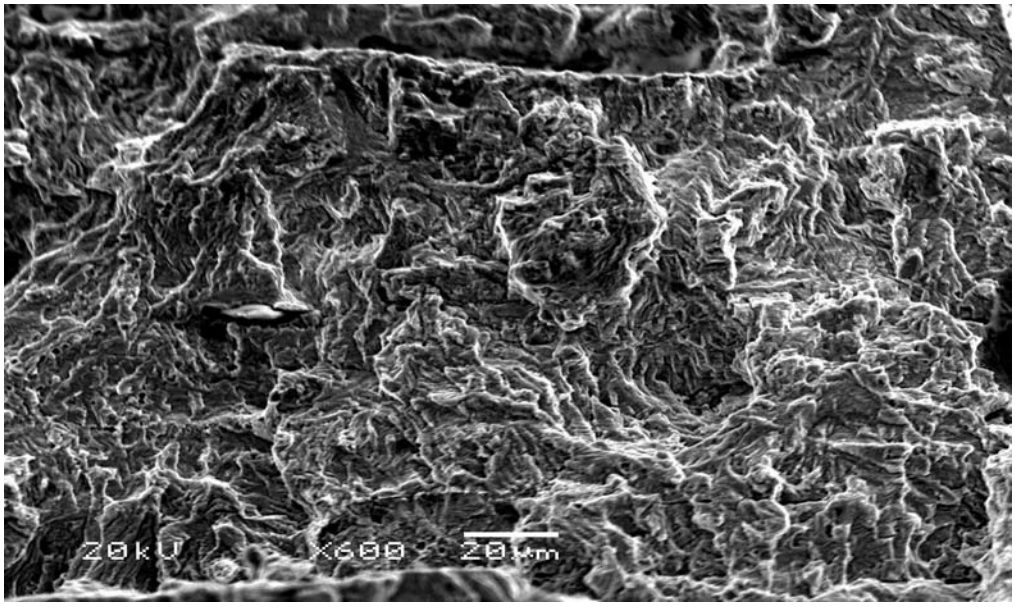

Figure 5.10- Fatigue Surface (High Magnification)

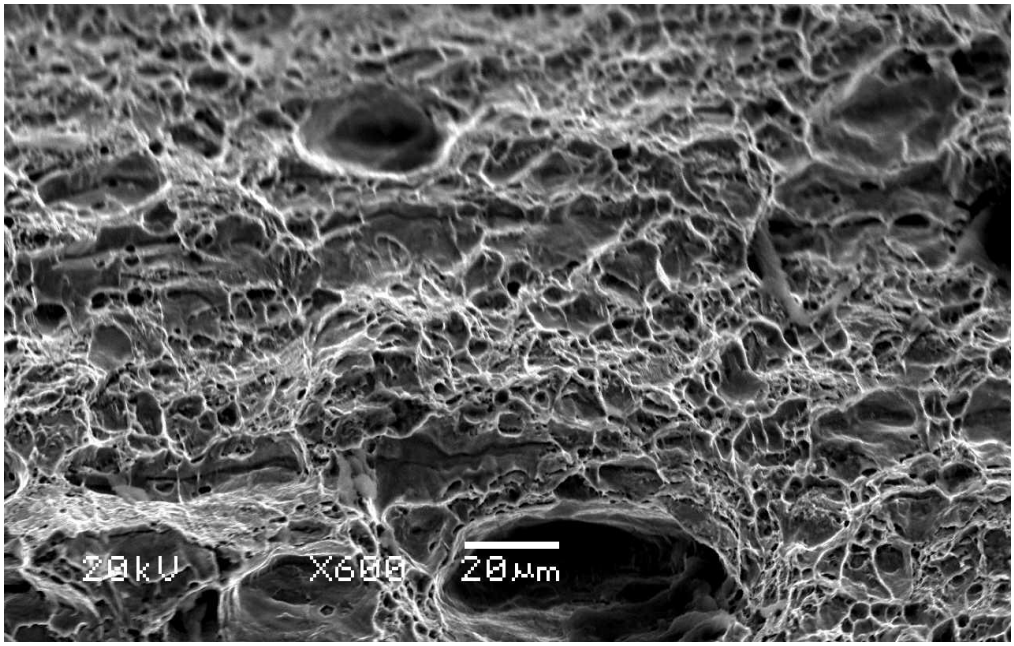

Figure 5.11- Ductile Fracture Surface (High Magnification)

5.3 Crack in Corrosion Defects (CIC)

Five burst tests were carried out on end-capped and seam-welded pipe specimens to investigate the failure behavior of axial CIC flaws in pipelines. These burst tests were carried out with varying defect depths and the test matrix shown in Table 5.5.

Table 5.5- Geometry and Results of Pipes Tested for CIC Defects

Test ID	Defect Length (mm)	Corrosion Width (mm)	Defect Depth		Total Defect Depth (%WT)	Experimental Failure Pressure (MPa)
			Crack (% d2)	Corrosion (% d1)		
CIC1	200	30	32	68	52	7.74
CIC2	200	30	38	62	59	6.72
CIC3	200	30	34	66	60	7.06
CIC4	200	30	30	70	61	7.89
CIC5	200	30	35	65	66	6.15

A typical defect cross section is shown in Figure 5.12.

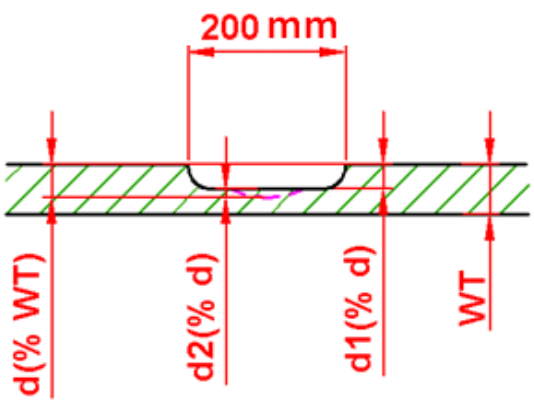

Total defect depth (d) =
Corrosion depth (d1) + Crack depth (d2)

Figure 5.12- Transverse View through CIC Flaw and Definition of Depth

The experimental failure pressures are shown in Figure 5.13. As explained in Chapter 4, the corrosion depth for CIC defects was intended to be equal to the initial slit depth. However, the corrosion depth for CIC4 (61% WT) was 0.2 mm less than initial slit depth and hence less material was removed compared to the other samples with the same depths (almost 60% WT). Therefore, as shown in Figure 5.13, the failure pressure for CIC4 was higher than the other samples of similar geometry. This will be reviewed more in detail later.

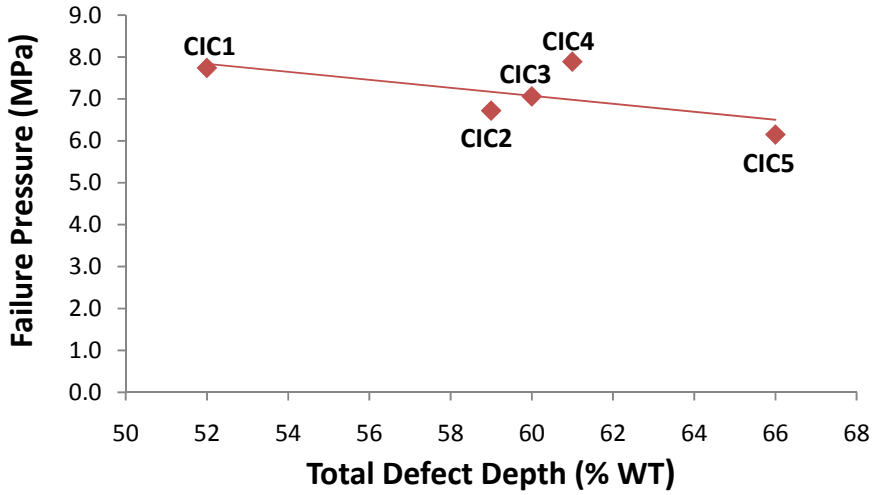

Figure 5.13- Experimental Results for CIC Defects

It was found that the failure pressure for CIC defects varied between a long uniform depth crack and long uniform corrosion defect [9]. Therefore, to predict the failure pressure of a CIC defect, two different assessment methods were employed:

1-The CIC defects were assumed to be crack defects of equivalent depths and lengths.

2-The CIC defects were assumed to be corrosion defects of equivalent depths and lengths.

Although the FAD approaches were developed for crack like flaws, they may be applied directly to the CIC defects. Previously it was found that level 3 FAD for API 579 cylinder and CorLAS were the best methods for assessing crack flaws. Therefore, these methods were applied to evaluate CICs, assuming they could be treated as crack defects of equivalent depths. On the other hand, as shown in the previous section, the RSTRENG was the best reliable method for evaluating artificial corrosion defects with a flat bottomed profile. Therefore, it was used to evaluate the CIC defects, assuming they could be treated as corrosion defects of equivalent depths.

The comparison between crack, corrosion and CIC defects is shown in Figure 5.14.The results also are shown in Table 5.7 and Figure 5.15:

Table 5.6- Comparison between the Experimental and the Predicted Failure Pressures

Test ID	Total Defect Depth (% WT)	Exp. Failure Pressure (MPa)	Predicted the Failure Pressure of Equivalent Defect (MPa)			$Error(\%) = \frac{Exp. - Pred.}{Exp.} \times 100$		
			Crack Only		Corrosion Only	Crack Only		Corrosion Only
			Level 3 FAD API 579-Cylinder	CorLAS	RSTRENG	Level 3 FAD API 579-Cylinder	CorLAS	RSTRENG
CIC1	52	7.74	6.15	7.21	6.55	21.0	7.0	15.0
CIC2	59	6.72	4.89	6.48	5.75	27.0	4.0	14.0
CIC3	60	7.06	4.75	6.45	5.63	33.0	9.0	20.0
CIC4	61	7.89	4.45	6.43	5.51	44.0	19.0	30.0
CIC5	66	6.15	3.73	5.93	4.91	39.0	4.0	20.0
				Average Error (%)		**33.0**	**8.0**	**20.0**

t	Pipe Thickness
L	Defect Length
d	Total Defect Depth
d1	Initial Slit Depth

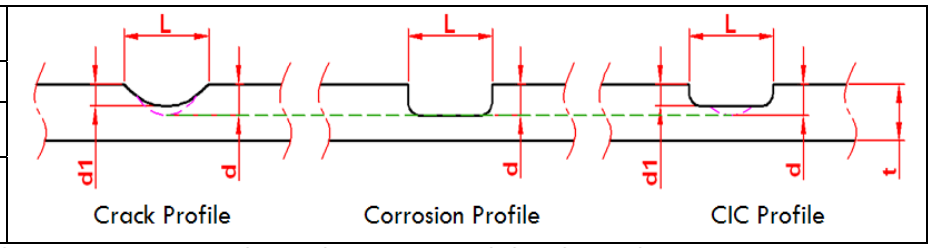

Figure 5.14- Comparison between Crack, Corrosion and CIC Defects of Equivalent Depths

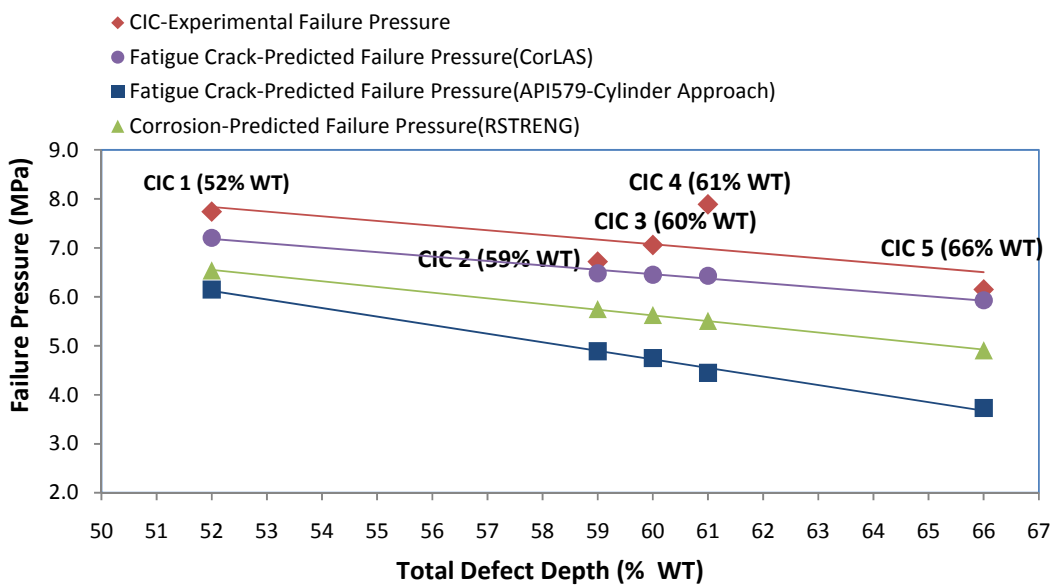

Figure 5.15- Comparison of the Experimental Failure Pressure and Analytical Crack and Corrosion Predicted Failure Pressures of Equivalent Depths for CIC Defects

All the methods provided conservative results for CIC defects and a review of the results in Figure 5.15 shows that CorLAS gave the more accurate results compared to RSTRENG and the level 3 FAD API 579.

In general, corrosion defects are less critical than crack flaws of equal depths. The corrosion defects are considered blunt defects whereas the crack defects are sharp defects. Therefore, it is expected that the failure pressure for the corrosion defects are higher than the crack defects of equivalent depths. However, as shown in Table 5.7, this is not the case for all the times. In addition to the depth, the geometry of the corrosion and crack defects should be considered when assessing the failure pressure.

As shown in Table 5.7, the failure pressures are given for two different corrosion profiles of equivalent depth. The failure pressure corresponding to the semi-elliptical profile, resembling a crack profile, is higher than that corresponding to a rectangular profile. More material removed in the second profile.

Table 5.7- Predicted Failure Pressure for Two Different Corrosion Defects with an Equivalent Depth

Profile ID	Pipe Thickness (mm)	Pipe Diameter (mm)	Corrosion Depth (%WT)	Corrosion Profile	Failure Pressure (RSTRENG) (MPa)
1	5.7	508	66	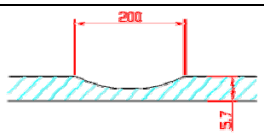	6.46
2	5.7	508	66	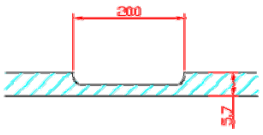	4.91

It was found that the failure pressure for the CIC defects fell between that of a long uniform deep crack and a long uniform deep corrosion defect, and it is expected that a transition failure behavior from the crack defect to the corrosion defect occurs when the crack to corrosion ratio is less than 25% [9]. However, a

review of the results in Figure 5.16 indicates that the crack to corrosion ratio is not the only parameter to evaluate a CIC defect. Defect depth and defect profile affect the failure behavior of a CIC defect. For instance, the total defect depth for both CIC1 (32%Cr+68% C) and CR4 (Crack only) are 52% and 51% WT resulted in experimental failure pressures of 7.74 MPa and 8.83 MPa respectively. The failure behavior of a CIC defect with the crack to corrosion ratio of 47% and a crack defect with an equal depth was not the same. More material being removed in the CIC defect led to an increased local stress at the crack tips.

Figure 5.16 summarizes all the experimental failure pressures for crack, corrosion and CIC defects.

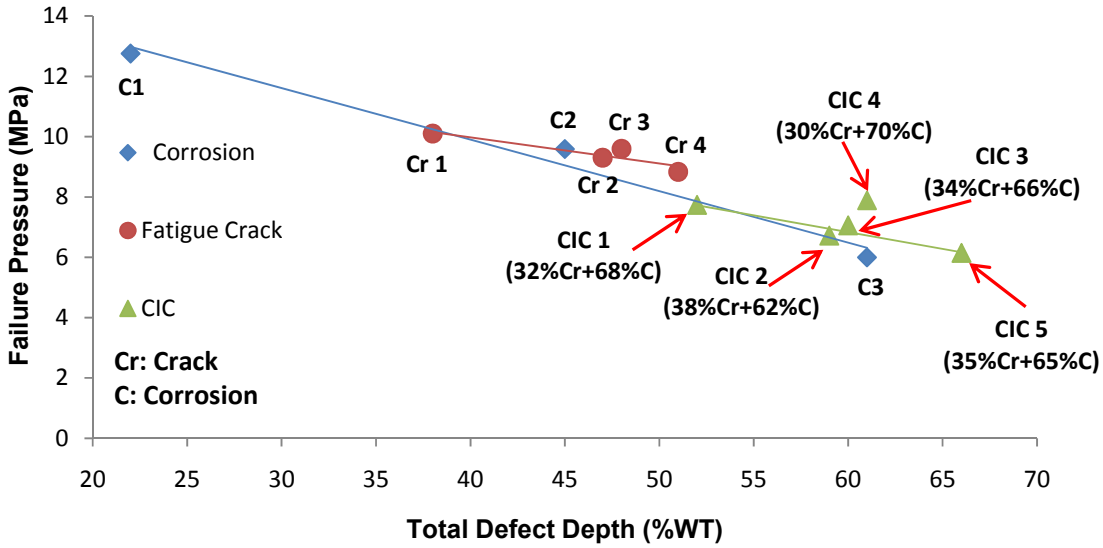

Figure 5.16-Comparing the Experimental Failure Pressures for Artificial Corrosion, Crack and CIC Defects

A review of the results in Figure 5.16 shows that the failure behavior of the CIC defects fell between corrosion defects (lower bound) and crack defects (upper bound) of equivalent depth. The transition to crack defect behavior only occurs when the crack defect depth is significant or vice versa. Moreover, failures for all CIC defects occurred by plastic collapse, verified by examining the fracture surfaces.

6. Summary, Conclusions and Recommendations

6.1 Summary

Crack-like flaws may occur coincident with corrosion in a pipeline and represent a defect named crack in corrosion (CIC). These crack in corrosion (CIC) defects have been identified in operating natural gas lines and there is a need to provide assessment and evaluate the integrity of the line as well as identify requirements for defect repair. The failure behavior of crack, corrosion and crack in corrosion defects were considered individually in this study. The experimental failure pressure for these types of defects was compared with each other to investigate the influence of these kinds of defects on the failure of pipelines.

Burst tests were undertaken in order to investigate the failure behavior of axially surface artificial corrosion defects in pipelines and access the applicability of the RSTRENG and Modified B31G methods. The total defect depths were varied 22% to 61% wall thickness.

Burst tests were successfully completed in order to investigate the failure behavior of axially oriented surface crack flaws in pipelines. The total defect depths varied 38% to 51% of the wall thickness. The results were used to assess the applicability of the level 3 FAD approach, NG-18 method and CorLAS in predicting failure.

Burst tests with total defect depths 52% to 66% wall thickness with crack to corrosion depth ratios of 43% to 61% were undertaken to evaluate CIC defects in pipelines and the applicability of the crack and corrosion assessment methods for CIC defects.

The current study considered finite length crack defects within long and finite length corrosion defects. The collapse pressure of a finite length crack within a corrosion defect was lower than a crack of equivalent total depth and length. This reduction in collapse pressure was attributed to increased local stresses in the

vicinity of the crack due to the coincident corrosion. The predicted collapse pressure increased towards the crack-only value when the length of the corrosion defect was decreased or the crack to corrosion ratio decreased.

For crack only defects, CorLAS provided the best estimate among other methods such as level 3 FAD or NG 18 method. For artificial corrosion only defects, RSTRENG provided the best estimate in comparison with Modified B31G.

6.2 Conclusions

The results showed that the predicted failure pressures based on RSTRENG were more reliable than the Modified B31G. The Modified B31G overestimated the failure pressure for deeper defect (i.e. 60% WT), whereas RSTRENG uses a more complete description of the geometry of the real corrosion defect in comparison with M B31G. The results showed that the failure of the artificial corroded pipes occurred due to the plastic collapse by ductile tearing.

The predicted collapse pressure from the level 3 FAD for the API 579 cylinder equations and CorLAS showed very good agreement with the experimental results. The level 3 FAD approach using API 579 cylinder equations also showed good agreement with experimental results. NG-18 provided conservative collapse pressure predictions and the degree of conservatism depended on the material properties and defect dimensions. The BS 7910 cylinder approach was the most conservative method. The failures for all crack-like defects (38%, 47%, 48% and 51% WT) were expected to occur by plastic collapse and were verified by examining the fracture surfaces.

The results showed that the failure behavior of the CIC defects fell between those of artificial corrosion defects and crack defects of equivalent depth. The transition to crack defect behavior occurred when the crack to corrosion ratio was greater than 75%. The transition to corrosion defect behavior occurred when the corrosion to crack ratio was greater than 75%. The examination of fracture surfaces showed that the failures for all defects occurred by plastic collapse.

The crack to corrosion ratio is an important parameter in CIC defects. However, it is not the only parameter to evaluate a CIC defect. There are other parameters such as defect depth and defect profile which affect to the failure behavior of a CIC defect.

6.3 Recommendations

It is recommended more detailed studies and corresponding experimental data are required to validate new methods and understand the applicability of existing methods to CIC defects. This study has demonstrated application of existing crack evaluation techniques to CIC and highlighted the need for improved measures of material properties. In particular, one of the largest gaps in knowledge is the material toughness, which is used in the evaluation techniques for thin-walled pipes. A parametric study should be undertaken to complement experimental methods, using numerical modeling techniques to predict failure using a two criterion approach (plastic collapse based on ligament stress, and fracture based on J).

References

[1] Canadian Energy Pipeline Association, www.cepa.com, September 2009.

[2] Association of Oil Pipe Lines, www.aopl.org, September 2009.

[3] American Petroleum Institute, "Recommended Practice for Fitness for Service", API -579, 2000.

[4] British Standards Institute, BS 7910. "Guide on Methods for Assessing the Acceptability of Flaws in Metallic Structures", BSI-10 2000.

[5] A.K. Escoe,"Piping and Pipeline Assessment Guide", Elsevier, 2006.

[6] D.S. Cronin and A. Plumtree, "Assessment of Crack in Corrosion Defects in natural Gas Transmission Pipelines", Confidential report to TCPL, November 30, 2007.

[7] D.S. Cronin and A. Plumtree, "Assessment of Crack in Corrosion Defects in natural Gas Transmission Pipelines", Confidential report to TCPL, November 28, 2006.

[8] Canadian Energy Pipeline Association (CEPA), "Stress Corrosion Cracking Recommended Practices, 2nd Edition", 2007.

[9] D.S. Cronin and A. Plumtree, "Assessment of Crack in Corrosion Defects in natural Gas Transmission Pipelines", 7th International Pipeline Conference (September29-October 3, 2008).

[10] G.R.K. Kanters, W.A." ,Pipeline Corrosion and Cracking and the Associated Calibration Considerations for Same Side Sizing Applications ",Eclipse Scientific Products Inc., Williams ford, Ontario, Canada.

[11] D.S. Cronin, "Assessment of Corrosion Defects In Pipelines", PhD Thesis, University Of Waterloo, 2000.

[12] W.L. Mercer, "Materials Requirements for Pipeline Construction", Series A, Mathematical and Physical Sciences, 1976.

[13] A. Cosham, P. Hopkins."Best Practice for the Assessment of Defects in Pipelines-Corrosion", Engineering Failure Analysis, 2007, 1245-1265.

[14] G. Glinka, "Course Notes ME627, Fatigue & Fracture Mechanics Analysis & Design", Fall 2007.

[15] N.E. Dowling, “Mechanical Behavior of Materials”, Pearson Education, Third Edition, 2007.

[16] European SINTAP Procedure,” Fitness-for-Service Fracture Assessment of Structures Containing Cracks”, 2007.

[17] CorLAS User Manual.

[18] Carl E. Jaske and John A. Beavers.,” Fitness-For-Service Evaluation of Pipelines with Stress-Corrosion Cracks or Local Corrosion”, The International Conference on Advances in Welding Technology (ICAWT), October 1999.

[19] C.F. Shih and J. W. Hutchinson, “Fully Plastic Solutions and Large Scale Yielding Estimates for Plane Stress Crack Problems,” Report No. DEAP S-14, Harvard University, Cambridge, MA, July, 1975.

[20] American Society for Testing and Materials (ASTM) Standards, ASTM E8M, 2007.

[21] CSA, ”CSA Z245-99,Oil and Gas Pipeline Systems”, CSA, Toronto, 1999

[22] D.R. Askeland, “The Science and Engineering of Materials”, Chapman & Hall, Third Edition, 1996.

[23] American Society for Testing and Materials (ASTM) Standards, ASTM E23, 2007.

[24] Badr. Bedairi, Master of Science Student in University of Waterloo.

[25] Efunda, Fracture Mechanics, http://www.efunda.com/formulae/formula_index.cfm, June 2008.

[26] J. Scheuring, “Introduction to the MTS Testing Machine in the Fatigue & Fracture Lab at Purdue University”, March 1, 1999.

[27] Controller 406 User Manual, MTS System Corporation.

[28] American Society for Testing and Materials (ASTM) Standards, ASTM E1820, 2008.

[29] University of Western Australia, http://www.mech.uwa.edu.au/DANotes/MST/thin/thin.html, October 2009.

[30] RoyMech, http://www.roymech.co.uk/Useful_Tables/Beams/Beam_energy_methods.html, July 2008.

[31] R.K. Watkins and L. R. Anderson, “Structural Mechanics of Buried Pipes”, CRC Press, 2000.

[32] P. Paris and F. Erdogan. “A Critical Analysis of Crack Propagation Laws J. Basic Eng.”, 85:528-543, 1963.

[33] M. Thomas, “Crack Growth in API X-60 Line Pipe Steel in NS4 Solution”, M.A.Sc. Thesis, University of Waterloo.

[34] T.L. Anderson, “Fracture Mechanics Fundamental and Application”, Taylor & Francis, Third Edition, 2005.

[35] American Gas & Chemical Co. Ltd. http://www.amgas.com/penpage.htm

[36] ESAB,http://www.esabna.com/us/en/education/knowledge/weldinginspection/Surface-Crack-Detection-of-Welds.cfm, March 2008.

[37] J.R. Gordon, “A Comparison of Methods of Calculating Stress Intensity Factors for Cracks in Pipes and Thin Walled Cylinders”, UK, 1998.

[38] D.S. Cronin and K. Andrew Roberts and R. J. Pick,” Assessment of Long Corrosion Grooves in Line Pipe” Department of Mechanical Engineering , University of Waterloo.

[39] Turnbull, McCartney, and Zhou, “Modeling of the evolution of stress corrosion cracks from corrosion pits”, Scripta Materialia 54 (2006) 575–578.

[40] K. Jones, and D., Hoeppner, “Pit-to-crack transition in pre-corroded 7075-T6 aluminum alloy under cyclic loading” Corrosion Science 47 (2005) 2185–2198.

[41] Medved, Breton and Irving, “Corrosion pit size distributions and fatigue lives-a study of the EIFS technique for fatigue design in the presence of corrosion”, International Journal of Fatigue 26 (2004) 71–80.

[42] R.N. Parkins, “Localized Corrosion and Crack Initiation”, Materials Science and Engineering, A 103 (1988) 143-156.

[43] I. M. Dmytrakh, “Corrosion Fatigue Cracking and Failure Risk Assessment of Pipelines”, Karpenko Physico-Mechanical Institute of National Academy of Sciences of Ukraine, 5 Naukova Street, 79601, Lviv, Ukraine.

Appendices

Appendix A

A. Reference Stress

A.1 API 579-Cylinder Approach

Reference stress for a cylinder under internal pressure containing a semi-elliptical surface crack may be calculated as follows :(taken from Appendix D section D.5.10 of API 579 [API 2000]) [1]. A sample cylinder is shown in Figure A.1.

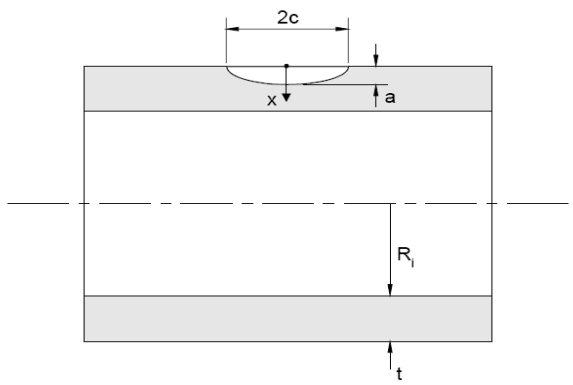

Figure A.1- Cylinder – Surface Crack, Longitudinal Direction-Semi-elliptical Shape [1]

It should be noted that there is no bending stress in this case; therefore the reference stress can be written as follows:

$$\sigma_{ref} = M_s \mathrm{P_m}$$

Where

P_m: Hoop Stress

Folios bulging factor $M_s$is given by:

$$\mathrm{M_s} = \frac{1-0.67\frac{a}{t}(\frac{1}{M_t})}{1-0.67\frac{a}{t}}$$

$$M_t = \frac{1.02+0.4411\lambda^2+.006124\lambda^4}{1+.02642\lambda^2+1.533X10^{-6}\lambda^4}$$

$\lambda = \frac{1.818C}{\sqrt{tR_i}}$

A.2 BS 7910-Cylinder Approach

Reference stress for a cylinder under internal pressure containing semi-elliptical surface crack may be calculated as follows:(taken from Appendix P section P.4.3.5 of BS 7910 [BSI 2000]) [4]. A sample cylinder is shown in Figure A.1.

$$\sigma_{ref} = 1.2M_s\mathrm{P_m}$$

Where

$$M_s = \frac{1-\{\frac{a}{t\mathrm{M_t}}\}}{1-\frac{a}{t}}$$

$$\mathrm{M_t} = \{1 + 1.6\left(\frac{\mathrm{c}^2}{2\mathrm{R_i t}}\right)\}^{0.5}$$

Appendix B

B. Stress Intensity

B.1 API 579-Cylinder Approach

Stress intensity for a cylinder under internal pressure containing semi-elliptical surface crack may be calculated as follows :(taken from Appendix C section C.5.10 of API 579 [API 2000]) [1]. A sample cylinder is shown in Figure A.1.

$$K_I = \frac{\mathrm{PR_i^2}}{\mathrm{R_o^2 - R_i^2}}[2G_0 + 2G_1(\frac{a}{\mathrm{R_i}}) + 3G_2(\frac{a}{\mathrm{R_i}})^2 + 4G_3(\frac{a}{\mathrm{R_i}})^3 + 5G_4(\frac{a}{\mathrm{R_i}})^4]\sqrt{\frac{\pi a}{Q}}$$

The influence coefficients G_0 and G_1 for inside and outside surface cracks can be determined using the following equations:

$$G_0 = \mathrm{A}_{0,0} + \mathrm{A}_{1,0}\beta + \mathrm{A}_{2,0}\beta^2 + \mathrm{A}_{3,0}\beta^3 + \mathrm{A}_{4,0}\beta^4 + \mathrm{A}_{5,0}\beta^5 + \mathrm{A}_{6,0}\beta^6$$

$$G_1 = \mathrm{A}_{0,1} + \mathrm{A}_{1,1}\beta + \mathrm{A}_{2,1}\beta^2 + \mathrm{A}_{3,1}\beta^3 + \mathrm{A}_{4,1}\beta^4 + \mathrm{A}_{5,1}\beta^5 + \mathrm{A}_{6,1}\beta^6$$

Where

β Is given by following Equation and the parameters A_{ij}, are provided in Table C.11.

$$\beta = \frac{2\varphi}{\pi}$$

The G_2 ,G_3 and G_4 influence coefficients can be computed using paragraph C.14.3 or C.14.4.

Q is determined using following equation:

Q=1+1.464 $(\frac{a}{c})^{1.65}$

σ_0: Uniform coefficient for polynomial stress distribution (MPa or psi)

B.2 BS 7910-Cylinder Approach

Stress intensity for a cylinder under internal pressure containing semi-elliptical surface crack may be calculated as follows :(taken from Appendix M section M.4.2 of BS 7910 [BSI 2000]) [4]. A sample cylinder is shown in Figure A.1.

$$K_I = \mathrm{Mf_w M_m} \sigma_\mathrm{m} \sqrt{\pi a}$$

Where

$$f_w = \{\sec\left(\frac{\pi a c}{\mathrm{tW}}\right)\}^{0.5}$$

$$\mathrm{M} = \frac{1-\{\frac{a}{t\mathrm{M_t}}\}}{1-\frac{a}{t}}$$

$$\mathrm{M_t} = \{1 + 3.2\left(\frac{\mathrm{c}^2}{2\mathrm{R_m t}}\right)\}^{0.5}$$

$$\mathrm{M_m} = \left\{\mathrm{M}\left\{\mathrm{M_1} + \mathrm{M_2}\left(\frac{a}{\mathrm{t}}\right)^2 + \mathrm{M_3}\left(\frac{a}{\mathrm{t}}\right)^4\right\}\mathrm{gf_\varphi f_w}\right\}/\mathrm{Q}$$

$$\mathrm{M_1} = 1.13 - 0.09\left(\frac{a}{c}\right)$$

$$\mathrm{M_2} = \frac{0.89}{0.2 + \left(\frac{a}{c}\right)} - 0.54$$

$$\mathrm{M_3} = 0.5 - \frac{1}{0.65 + \left(\frac{a}{c}\right)} + 14\{1 - \left(\frac{a}{c}\right)\}^{24}$$

$$\mathrm{Q} = \{1 + 1.464\left(\frac{a}{c}\right)^{1.65}\}^{0.5}$$

In our case:

For deep point:

$g = 1$

$\mathrm{f_\varphi} = 1$

For surface point:

$$g = \{1.1 + 0.35\left(\frac{a}{t}\right)^2\}$$

$$\mathrm{f}_{\varphi} = \left(\frac{a}{c}\right)^{0.5}$$